PONTIFICIA
UNIVERSIDAD
CATÓLICA
DE CHILE

FACULTAD DE FISICA
INSTITUTO DE ASTROFISICA

DUSTY CLUMPS IN CIRCUMBINARY DISCS

by

PEDRO PABLO A. POBLETE RIVERA

Thesis presented to the Faculty of Physics of the
Ponticifia Universidad Católica de Chile, to apply
for the academic degree of Master in Astrophysics.

Advisor	:	Dr. Nicolás Cuello (PUC Chile)
Co-advisor	:	Dr. Jorge Cuadra (PUC Chile)
Correctors	:	Dr. Viviana Guzmán (PUC Chile)
		Dr. Myriam Benisty (CNRS UChile Chile)

October, 2019
Santiago, Chile

"In the midst of chaos, there is also opportunity."

Sun Tzu

Acknowledgements

I want to thank my family for being by my side in this process, my sister and my parents. They never abandoned me and were always there for when I needed it most. To my friends, both those of the university and those of my hometown Talca, for encouraging me and giving me their help when I requested them. Also, thank the professors of the Institute of Astrophysics, Nicolás Cuello and Jorge Cuadra, because they were and are a fundamental piece in my career as an astronomer.

I also thank the anonymous referee for valuable comments and suggestions that have improved this work. Figures 3.1, 3.2, 3.6, 3.4, 4.2, 4.3, 4.4, 5.1(b), and 5.2 were made with SPLASH (Price, 2007). The Geryon2 cluster housed at the Centro de Astro-Ingenieria UC was used for the calculations performed in this work. The BASAL PFB-06 CATA, Anillo ACT-86, FONDEQUIP AIC- 57, and QUIMAL 130008 provided funding for several improvements to the Geryon/Geryon2 cluster. The author acknowledge support from CONICYT project Basal AFB-170002. The author acknowledge financial support provided by NPF.

Abstract

Protoplanetary discs are structures formed by gas and dust that form during the first stages of the stellar evolution. Protoplanetary discs also are the birthplace of planets, moons, and asteroids like the ones we observe in our Solar System. However, protoplanetary disc structure varies amongst different systems. A good understanding of disc evolution and dynamics is required for a comprehensive view of planet formation. Recent observations have revealed that protoplanetary discs often exhibit cavities and azimuthal asymmetries such as dust traps and clumps. The presence of a stellar binary system in the inner disc regions has been proposed to explain the formation of these structures. In that case, the protoplanetary disc should be reclassified as circumbinary. Here, I study the dust and gas dynamics in circumbinary discs around eccentric and inclined binaries. This is done through two-fluid simulations of circumbinary discs, considering different values of the binary eccentricity and inclination. The simulations are made using PHANTOM; a three-dimensional smoothed particle hydrodynamics code. I find that two kinds of dust structures can form in the disc: a single horseshoe-shaped clump, on top of a similar gaseous over-density; or numerous clumps, distributed along the inner disc rim. The latter features form through the complex interplay between the dust particles and the gaseous spirals caused by the binary. All these clumps survive between one and several tens of orbital periods at the feature location. I show that their evolution strongly depends on the gas–dust coupling and the binary parameters. Interestingly, these asymmetric features could in principle be used to infer or constrain the orbital parameters of a stellar companion — potentially unseen — inside the inner disc cavity. Finally, I apply these findings to the disc around AB Aurigae. The dusty clumps observed in this work suggest that circumbinary discs are promising places to form planetesimals and even planets, contrary to what was previously thought due to high relative velocity among solids.

Contents

List of Figures

Chapter 1

Introduction

In the last years, the field of planet formation has experienced an unprecedented development thanks to last-generation telescopes. In particular, by combining multi-wavelength observations of protoplanetary discs (PPDs) – the place where planets form – it has been possible to map the dust distribution for a wide range of grain sizes, and the different layers of discs around young stars (See Figure 1.1). Extreme adaptive optics instruments in large optical/NIR (near infrared) telescopes, such as SPHERE/VLT, and radio antennas (mainly ALMA) observing at mm and submm wavelengths played a key role in achieving this task. This shed some light on the very first stages of planet formation within these systems (Avenhaus et al., 2018; Pinilla et al., 2018). Among the now overwhelming number of ALMA observations of protoplanetary discs, the continuum emission detected around HL Tau is one of the most spectacular (ALMA Partnership et al., 2015); it showed concentric rings and gaps. Particularly, the numerous gaps observed suggest that planets might have already formed in this young disc (Dipierro et al., 2015b). Signatures of planet-disc interactions have also been observed in PDS 70 (Isella et al., 2019) and HD 163296 (Isella et al., 2018; Pinte et al., 2018). Besides the routinely detected gaps, there are also numerous observations of enigmatic structures such as, spirals (Benisty et al., 2015, 2017; Pérez et al., 2016; Huang et al., 2018), warps (Langlois et al., 2018; Casassus et al., 2018b; van der Plas et al., 2019), horeshoes (van der Marel et al., 2013; Boehler et al., 2017), clumps (Dong et al., 2018; Gratton et al., 2019), shadows (Avenhaus et al., 2014; Stolker et al.,

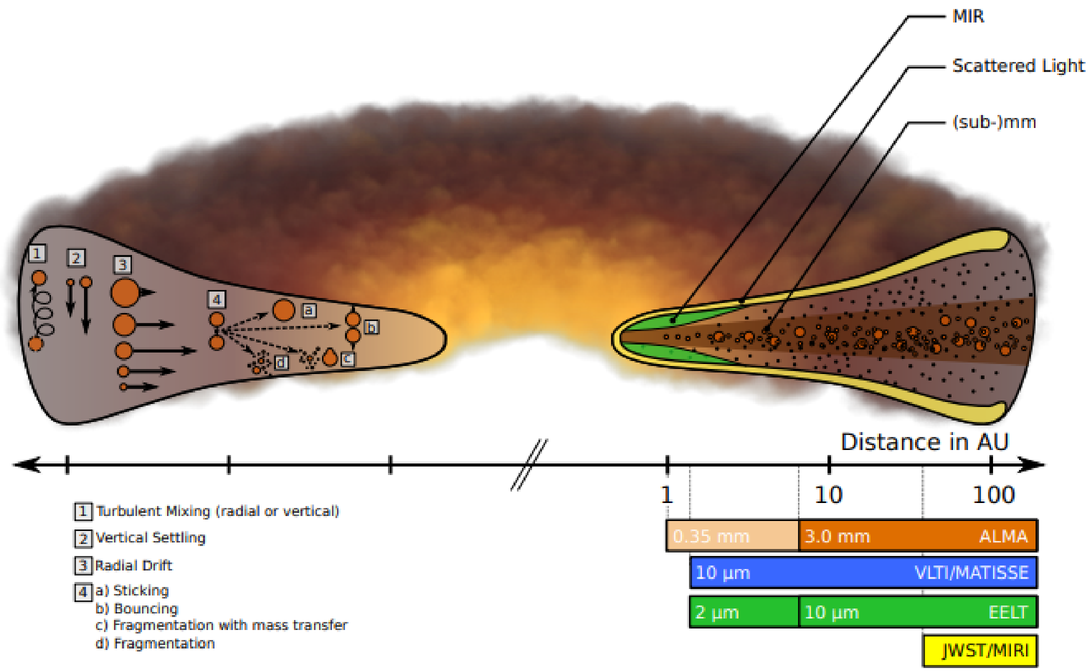

Figure 1.1: Illustration of the structure, grain evolution processes and observational constraints for protoplanetary disks. On the left side it shows the main grain transport and collision mechanism properties. The different lengths of the arrows illustrate the different velocities of the different grains. On the right hand side, it shows the areas of the disk that can be probed by the various techniques. The axis shows the logarithmic radial distance from the central star. The horizontal bars show the highest angular resolutions (left edge of the bars) that can be achieved with a set of upcoming facilities and instruments for at the typical distance of the nearest star forming regions. Picture taken from Testi et al. (2014) Figure 1.

2016; Benisty et al., 2018), and rings (ALMA Partnership et al., 2015; Tsukagoshi et al., 2016; Dipierro et al., 2018; Andrews et al., 2018). Remarkably, the recent DSHARP survey by Andrews et al. (2018) mapped twenty nearby protoplanetary discs at an astonishing resolution of roughly 5 au. However, the rich structure of these systems remains only partly understood from the theoretical point of view (Armitage, 2018).

When the gas cloud collapses and stars start to form, protoplanetary discs are created. These structures are composed by a mixture of gas and solid material (dust plus ices). The gas is mainly molecular hydrogen (H_2). The main disc structure parameters are its radial extension, its aspect-ratio (H/R), and its temperature and surface density. Temperature and surface density usually are modeled as power laws. The stars at early formation stages are not main sequence stars yet, and thus they are called young stellar objects (YSO). YSOs are usually split into four classes: Class 0, I, II, and III (Lada, 1987; Williams & Cieza, 2011). This classification is based on the excess of the infrared emission observed in the spectral energy distribution (SED) of the unresolved source (star plus disc). Protoplanetary discs mainly appear in Class I and II stages. The main difference between both is that in Class II, the gas envelope has practically vanished. Multiplicity in YSOs (two or more in the same system) is very common (Duchêne & Kraus, 2013; Reipurth et al., 2014). Nevertheless, an important fraction of them becomes single systems due to three-body interactions and eventually ejection of one or more YSOs that compose it. Even so, a considerable quantity of YSOs remains, at least, as binaries. These constitute a special category of protoplanetary discs called *circumbinary*. Considering the stellar context, roughly half of the solar-type stars are single, whereas about 33% of them form double systems (Raghavan et al., 2010; Tokovinin, 2014). Therefore, about a third of the young stellar systems could potentially harbour circumbinary discs (CBDs), along with circumstellar ones. Hence, a proper understanding of circumbinary disc dynamics is of crucial importance (Nixon et al., 2013; Dunhill et al., 2015; Cuello & Giuppone, 2019).

The case of the disc around HD 142527 is particularly enlightening in this regard. Fukagawa et al. (2006) first detected a disc with several spiral arms and a large inner cavity of roughly 90 au of radius. This disc was initially thought to be orbiting a single star. However, a companion was later discovered inside the inner cavity by Biller et al. (2012). The stellar masses in HD 142527 are 1.8 $M_{\odot}$ (Gaia Collaboration et al., 2016) and 0.4 $M_{\odot}$ (Christiaens et al., 2018), so it is an *unequal-mass binary*. Further studies focused on the companion's orbital motion (Lacour et al., 2016; Claudi et al., 2019) indicating that the binary is eccentric and likely inclined with respect with the disc. Based on these constraints, Price et al. (2018b) presented a consistent hydrodynamical model of HD 142527 where the CBD is periodically perturbed by the inner binary. Remarkably, the resulting gaseous and dust structures are in excellent agreement with all the available multi-wavelength observations:

i) The spirals and their location (Avenhaus et al., 2014; Christiaens et al., 2014).

ii) The cavity size (Perez et al., 2015).

iii) The dusty clumps along a horseshoe (Casassus et al., 2015b; Boehler et al., 2017).

iv) The gaseous filaments crossing the cavity (Casassus et al., 2013).

v) The shadows (Avenhaus et al., 2014) — likely caused by the presence of a misaligned inner disc (Marino et al., 2015).

Due to the high contrast in luminosity, detecting faint stars close to massive ones remains challenging. For this reason, the circumbinary scenario is currently most relevant for discs with large inner cavities exhibiting various asymmetries. Thereby, features in protoplanetary discs could be used as indicators of undetected stellar companions. For instance, Ragusa et al. (2017) explored how circular *unequal-mass binaries* ($M_2/M_1 = \{0.01, 0.05, 0.1, 0.2\}$) in a coplanar configuration are able to generate lopsided features and horseshoes at the edge of the cavity — comparable to the ones observed. Alternatively, the presence of vortices has been widely proposed to explain the same asymmetries in protoplanetary discs (Meheut et al., 2012; Lyra & Lin, 2013; Ataiee et al., 2013; van der Marel et al., 2016b). It is worth noting that, in the binary scenario, no vortex is required whatsoever. Regardless of their origin, these features are expected to efficiently trap dust in the inner disc regions (Birnstiel et al., 2013) due to their high gas density.

A comprehensive methodology, that connects the signatures of a binary system to its circumbinary disc can be applied to systems which exhibit highly structured discs with large inner cavities. This methodology motivates the search of possible unseen stellar companions. Examples of other systems of interest are mentioned in Table 1.1:

The aim of this work is to study the effect of an inclined and eccentric inner binary on the dust content of the surrounding CBD. To do so, I consider relatively high eccentricities ($e_\mathrm{B} = 0.5$ and $e_\mathrm{B} = 0.75$) and different inclinations for the binary respect to the disc, from prograde ($i_\mathrm{B} = 0°$) to retrograde ($i_\mathrm{B} = 180°$) configurations. In addition, I will establish a connection between the disc features caused by the binary and its orbital parameters. This is done for *unequal-mass binaries* using CBD parameters consistent with recent observations. The numerical method and the initial setup of our three-dimensional

System	Spiral Arms	Rings	Shadows	Dusty Clumps
AB Aurigae	multi	yes	no	more than one
DoAr 44	not reported	yes	yes	more than two
MWC 758	two	yes	no	one
HD 169142	three	yes	no	more than two
HD 135344	two	yes	yes	two

Table 1.1: Others systems with prominent and non-axisymmetric structures like HD 142527: AB Aurigae (Fukagawa et al., 2004; Corder et al., 2005; Tang et al., 2012; Rodríguez et al., 2014; Pacheco-Vázquez et al., 2016), DoAr 44 (van der Marel et al., 2016a; Casassus et al., 2018b), MWC 758 (Benisty et al., 2015; Boehler et al., 2018; Casassus et al., 2018a; Dong et al., 2018), HD 169142 (Pohl et al., 2017; Gratton et al., 2019; Pérez et al., 2019), and HD 135344 (van der Marel et al., 2016a; Stolker et al., 2016; Cazzoletti et al., 2018).

hydrodynamical simulations are described in Chapter 2. The simulations outcomes and numerical tests are reported in Chapter 3. In Chapter 4, I discuss the formation of dusty clumps, and their evolution. In Chapter 5, I describe how clumps can be used to infer the presence of a potentially unseen inner companion. Finally, I draw my conclusions and discuss future work in Chapter 6.

Chapter 2

Physical Model and Numerical Method

I perform 3D hydrodynamics simulations of circumbinary discs using the PHANTOM smoothed particle hydrodynamics code (Price et al., 2018a). I use the two-fluid method in order to model the interaction between gas and dust particles as described in Laibe & Price (2012a,b). Such method treats each fluid independently, except that gas and dust particles interact with each other through aerodynamical drag forces. This means that the back-reaction – dust drag on the gas – is included in the calculations. Finally, the central stars are modeled as sink particles. A detailed description of the mentioned methods is provided below.

2.1 PHANTOM code for hydrodynamic simulations

PHANTOM is a *Smoothed Particle Hydrodynamics* (SPH) code written in Fortran. The SPH method models continuum media, such as a fluid, through a finite set of Lagrangian particles. It is a meshfree method, and it is advantageous to model complex fluid dynamics since the position (and other physical fields) can evolve freely without boundaries.

The fundamental equations that PHANTOM solve are:

$$\frac{\mathrm{d}\vec{r}}{\mathrm{d}t} = \vec{v} \tag{2.1}$$

$$\frac{\mathrm{d}\rho}{\mathrm{d}t} = -\rho(\nabla \cdot \vec{v}) \tag{2.2}$$

The Equation (2.1) represents the Lagrangian update of a particle at the position $\vec{r}$, i.e., the evolution in the position of SPH particles. The Equation (2.2) is the continuity equation which represents the mass conservation, with ρ the density. The density is computed from a set of point-like particles. The set is built by a neighbor-finding algorithm. By default, PHANTOM employs the *kd-tree* method to create a group with a determined number of SPH particles. All particles have the same mass. In order to compute the density, it is necessary to verify some conditions: the solution must be independent of the absolute position of the particle, and it just has to depend on the relative separation among them. Also, the solution must conserve the angular momentum and independent of time or history of the particles. Then, the density – on SPH – is computed as the Riemann summation over the particles, as follows way:

$$\rho(\vec{r}) = \int \rho(\vec{k}) W(|\vec{r} - \vec{k}|, h) \ \mathrm{d}V(\vec{k}) \approx \sum_{i=1}^{N_{\text{neighbors}}} m_i W(|\vec{r} - \vec{r_i}|, h), \tag{2.3}$$

where V is volume, $N_{\text{neighbors}}$ represents the number of the SPH neighbor particles, W is the *smoothing kernel* (typically truncated Gaussian-like functions), and h is the *smoothing length*.

The *smoothing kernel* is the key parameter for discretizing any physical quantity on SPH. An arbitrary physical field (A) of any SPH particle (or a point in the space) can be computed summing over all the *neighbors* as follows:

$$A(\vec{r}) \approx \sum_{i=1}^{N_{\text{neighbors}}} A_i V_i \ W(|\vec{r} - \vec{r_i}|, h), \tag{2.4}$$

with V_i the volume of particle i.

In this work, I use three kinds of particles: gas particles, dust particles and sink particles. The latter one used to model the inner binary.

2.2 Binary setup

I consider a binary system where both stars are treated as sink particles (Bate et al., 1995). PHANTOM treats sink particles independently from others SPH particles. Sinks are able to interact with others particles, including another sink particle. The sink-sink interaction is computed as follows:

$$\vec{a}^{i}_{\text{sink}-\text{sink}} = -\sum_{j=1}^{n} \frac{GM_j}{|\vec{r}_i - \vec{r}_j|^3}\vec{r}_{ij} \tag{2.5}$$

Sink particles can accrete gas and they can store the accreted angular momentum and other extended properties, such as the accreted mass among others. Notwithstanding, the gas accetion rate is not discussed in this work.

Initial conditions of binaries

I explore a range of orbital parameters similar to those observed in HD 142527 (Price et al., 2018b). In particular, I test different combinations of binary inclination respect to the disc ($i_{\rm B}$) and eccentricity ($e_{\rm B}$). The mass ratio between the primary and the secondary stars is fixed at $q = M_2/M_1 = 0.25$, with $M_1 = 2\,M_\odot$ and $M_2 = 0.5\,M_\odot$. The semi-major axis is set to 40 au (as in Price et al. (2018b) for HD 142527B). The free parameters in my simulations are $e_{\rm B}$ and $i_{\rm B}$. In this work, I consider the following sets of values: $e_{\rm B} = \{0.50, 0.75\}$ and $i_{\rm B} = \{0^\circ, 30^\circ, 60^\circ, 90^\circ, 120^\circ, 150^\circ, 180^\circ\}$. I model each system for a hundred binary orbits ($\sim$11 Kyrs).

The accretion of the sink particles – and consequently the change of the binary momentum – is negligible during the hundred binary orbits considered. Therefore, the binary remains unchanged, and the parameters aforementioned can be considered as constant throughout each simulation. The whole setup of combinations of orbital parameters for the simulations will be discussed in more detail in Chapter 2.4.

2.3 Disc setup

I model the circumbinary disc with 10^6 gas particles and 10^5 dust particles, assuming a total gas mass of $0.01\,M_\odot$ and a dust-to-gas ratio of 0.01. The spatial distribution of both fluids is initially the same. As in Price et al. (2018b), I consider a disc setup consistent with the observations of HD 142527. I set the inner and the outer edges at $R_{\rm in} = 90$ au and $R_{\rm out} = 350$ au, respectively.

2.3.1 Gas modelling

I model the gas disc as a vertically isothermal disc, i.e. the temperature does not depend on the height. The equation to model such gas disc are:

$$\frac{\mathrm{d}\vec{v}}{\mathrm{d}t} = -\frac{\nabla P}{\rho} + \Pi_{\rm shock} + \vec{a}_{\rm ext}(\vec{r}, t). \tag{2.6}$$

Equation (2.6) contains the involved terms in the acceleration: P is the pressure, $\Pi_{\rm shock}$ is a dissipation term, and $\vec{a}_{\rm ext}(\vec{r}, t)$ represents accelerations due to external forces[1].

The external force term $\vec{a}_{\rm ext}(\vec{r}, t)$ is computed as:

$$\vec{a}_{\rm ext}(\vec{r}, t) = -(\nabla\Phi_1 + \nabla\Phi_2) = -\nabla\left(\frac{GM_1}{|\vec{r} - \vec{r}_1(t)|} + \frac{GM_2}{|\vec{r} - \vec{r}_2(t)|}\right), \tag{2.7}$$

where Φ is the Newtonian classic potential since I do not consider relativistic effects. M_1 and M_2 represent the mass of each star: the primary with 2 $M_\odot$ and the secondary with 0.5 $M_\odot$ respectively, and $\vec{r}_1(t)$ and $\vec{r}_2(t)$ their positions.

For two SPH particles a and b, Equation (2.6) is rewritten as:

$$\frac{\mathrm{d}\vec{v}_a}{\mathrm{d}t} = -\sum_b^{N_{\rm neighbors}} m_b \left[\frac{P_a + q^a_{ab}}{\rho_a^2\Omega_a}\nabla_a W_{ab}(h_a) + \frac{P_b + q^b_{ab}}{\rho_b^2\Omega_b}\nabla_a W_{ab}(h_b)\right] + \vec{a}_{\rm ext}(\vec{r}_a, t), \tag{2.8}$$

where q^a_{ab} and q^b_{ab} represent the artificial viscosity. The artificial viscosity controls the transport of linear and angular momentum of fluid. See Price et al. (2018a) for further

[1] In this case, the term corresponds to gravitational potential of the two inner stars.

technical details.

Besides, an equation of state is required to complete the gas modelling. The equation of state for vertically isothermal gas is given by:

$$P = c_s^2(T)\rho, \tag{2.9}$$

where c_s is the sound speed that depends on the temperature profile, which in this case is prescribed and constant throughout the runs (see below).

Initial conditions of gas disc

I set the gas initial surface density and temperature profiles. The values are taken from previous studies of HD 142527 disc as in Price et al. (2018b). Therefore, I use values in agreement with a realistic circumbinary disc. These profiles are defined as:

$$\Sigma(r) = 0.544 \left(\frac{r}{100 \text{ au}}\right)^{-1} \text{ gr cm}^{-2}, \tag{2.10}$$

$$T(r) = 27.9 \left(\frac{r}{100 \text{ au}}\right)^{-0.3} \text{ °K}. \tag{2.11}$$

I assume an initial power-law surface density profile of r^{-1}. The temperature profile has a decay of $r^{-0.3}$ in agreement with the estimated observational profile to HD 142527 in Casassus et al. (2015a).

2.3.2 Dust modelling

Dust is modelled simultaneously with gas using the two-fluids method described in Laibe & Price (2012a,b). In the two-fluid implementation, dust and gas are treated as two independent fluids coupled by a drag term. The continuity equation is the same for both gas (g) and dust (d), and they are:

$$\frac{\partial \rho_{\rm g}}{\partial t} + (\vec{v}_{\rm g} \cdot \nabla)\rho_{\rm g} = -\rho_{\rm g}(\nabla \cdot \vec{v}_{\rm g}), \tag{2.12}$$

$$\frac{\partial \rho_{\rm d}}{\partial t} + (\vec{v}_{\rm d} \cdot \nabla)\rho_{\rm d} = -\rho_{\rm d}(\nabla \cdot \vec{v}_{\rm d}). \tag{2.13}$$

The main difference between both species is that dust is a pressure-less fluid. Hence, the acceleration equations are given by:

$$\frac{\partial \vec{v}_{\rm g}}{\partial t} + (\vec{v}_{\rm g} \cdot \nabla)\vec{v}_{\rm g} = -\frac{\nabla P}{\rho_{\rm g}} + \frac{K}{\rho_{\rm g}}(\vec{v}_{\rm d} - \vec{v}_{\rm g}), \tag{2.14}$$

$$\frac{\partial \vec{v}_{\rm d}}{\partial t} + (\vec{v}_{\rm d} \cdot \nabla)\vec{v}_{\rm d} = \frac{K}{\rho_{\rm d}}(\vec{v}_{\rm d} - \vec{v}_{\rm g}), \tag{2.15}$$

where K is a drag coefficient. From these equation we can see that gas is also affected by dust. In other words, the method accounts for back-reaction.

Gas and dust coupling: stopping time and Stokes number

The most important aspect on the study of mixtures of gas and dust is the degree of aerodynamic coupling between these fluids. A first step to quantify the coupling degree is to define the stopping time. The stopping time (noted $t_{\rm s}$) is the time-scale for the drag to damp the local differential velocity between the gas and dust. It is a function of both densities as follows:

$$t_{\rm s} = \frac{\rho_{\rm g}\rho_{\rm d}}{K(\rho_{\rm g} + \rho_{\rm d})}. \tag{2.16}$$

When PHANTOM computes the stopping time, it has to determine the aerodynamic drag regime. This is governed by the term K. There are two regimes: the Stokes and the Epstein regimes; the choice is determined according to the local mixture conditions (Epstein, 1924). In simple terms, a dust particle is in the Stokes regime when roughly its mean free path in the gas is comparable with its size. If the mean free path is greater than its size, then the particle is in the Epstein regime. PHANTOM evaluates the Knudsen number (Stepinski & Valageas, 1996) to determine the drag regime. The Knudsen number is defined as:

$$K_{\rm n} = \frac{9}{4}\frac{\lambda_{\rm g}}{s_{\rm grain}}, \tag{2.17}$$

where $\lambda_{\rm g}$ is the mean free path of gas and $s_{\rm grain}$ is the dust grain size.

If $K_{\rm n} < 1$, the stopping time is computed following the Stokes regime; and it is computed in the Epstein regime if $K_{\rm n} \geq 1$. In all my simulations, the mean free path of the dust particles is greater than their size. Then, the drag force falls in the Epstein regime. The stopping time in the Epstein regime is computed using the prescription proposed by Dipierro et al. (2015b, 2016) and Price et al. (2018b):

$$t_{\rm s} = \frac{\rho_{\rm grain} s_{\rm grain}}{\rho_{\rm total} c_{\rm s} f}\sqrt{\frac{\pi\gamma}{8}}, \tag{2.18}$$

where $\rho_{\rm grain}$ is the intrinsic density of the dust grain, which is set by default to 3 gr/cm^3 (typical value for astrophysical silicate), $\rho_{\rm total}$ is the sum of the gas and dust volume densities ($\rho_{\rm g} + \rho_{\rm d}$), $c_{\rm s}$ is the sound speed, and f is a correction for supersonic drift velocities (Kwok, 1975). In this work, the code has been modified a bit ($\rho_{\rm total} = \rho_{\rm g}$) for computational convenience. This will be discussed in detail at the section 2.3.2.

Using the stopping time, we can define the Stokes number. The Stokes number is defined as the ratio of the drag stopping time to the orbital period:

$$\mathrm{St} = \frac{t_{\rm s}}{T_{\rm orb}} = t_{\rm s}\Omega_{\rm k}, \tag{2.19}$$

where $\Omega_{\rm k}$ is the Keplerian angular velocity. The Stokes number is a dimensionless parameter that quantifies the coupling between gas and dust. There are three regimes of coupling that can be differentiated by the value of the Stokes number (Weidenschilling, 1977):

i) Strong coupling ($\mathrm{St} \ll 1$): In this regime, dust behavior is similar to gas. Dust reacts easily to the changes in gas velocities. In typical PPDs, this regime is associated with small dust grains (of the order of 1 μm or less).

ii) Marginal coupling ($\mathrm{St} \sim 1$): It is an intermediate regime. Dust radial velocities strongly depends on the position of local pressure maximum of gas. The gas disc conditions affect which grain size range corresponds to this regime.

iii) Weak coupling (St $\gg$ 1): Dust feels little gas drag effects. In typical PPDs, dust moves in Keplerian motion and its radial velocity is not affected significantly. This regime is associated with large dust grains or planetesimals (of the order of 1 m or more).

As already mentioned, each regime has a dust grain size associated. In consequence, each regime has associated a specific wavelength emission too. Draine (2006) gives a useful relation between emission regime and dust grain size: $s_{\rm grain} \sim 3 \cdot \lambda$. Thus, small grains are typically observed in the near-infrared, whereas large grain sizes at radio frequencies.

The mathematical sustain of the mentioned properties above for each regime, can be obtained by analyzing the equations of motion of dust and gas particles. Consequently, the equation of motion for dust being affected by gas drag effects can be rewritten as a function of the Stokes number.

In the prescription of Takeuchi & Lin (2002), the angular dust velocity by gas drag effects, and assuming no radial drift is given by:

$$\frac{{\rm d}v_{\theta,{\rm d}}}{{\rm d}t} = -\frac{\Omega_{\rm k,mid}}{\rm St} \cdot (v_{\theta,{\rm d}} - v_{\theta,{\rm g}}), \tag{2.20}$$

where $\Omega_{\rm k,mid}$ es the Keplerian angular velocity at the mid-plane. We can identify two limits:

- When the Stokes number becomes very low (i.e. for small grains), the angular dust velocity is given by the gas angular velocity. Then, dust is strongly coupled to gas.

- When the Stokes number becomes very high (i.e. for big grains and planetesimals), the right term becomes negligible. Hence, gas does not affect the dust particles, and the dust motion is given by the central potential, i.e., Keplerian movement.

On the other hand, Takeuchi & Lin (2002) also give the following approximation for the dust radial velocity:

$$v_{\rm r,d} = \frac{1}{1+{\rm St}^2} \cdot v_{\rm r,g} - \frac{1}{{\rm St}+{\rm St}^{-1}} \cdot (\eta V_{\rm k,mid}), \tag{2.21}$$

where $V_{\rm k,mid}$ is the Keplerian velocity at the mid-plane, and η is a factor that quantifies the difference in gas velocity with respect to Keplerian velocity. The latter is given by:

$$\eta = 1 - \left(\frac{v_{\theta,\rm g}}{V_{\rm k,mid}}\right)^2 = -\frac{r}{V_{\rm k,mid}^2 \rho_{\rm g}} \left(\frac{\partial P_{\rm g}}{\partial r}\right). \tag{2.22}$$

It is worth to remark that the dust radial velocity does not only depend on the gas velocity, as Equation (2.20). The first term in Equation (2.21) represents the dust drift motion carried by gas flows, and the second term represents the drift motion by drag effect. The drag force triggers an exchange of angular momentum between gas and dust particles. In consequence, dust particles can migrate radially inward or outward depending on the local conditions. As shown in Equations (2.21) and (2.22), dust moves radially towards the gas pressure maxima.

The second term in Equation (2.21) gives 0 for both high and low values of the Stokes number. In addition, it has a global maximum at St = 1 (See Figure 2.1). Therefore, the radial drift due to gas drag is most when dust is marginally coupled to the gas: in this regime, the dust has the fastest radial drift (Weidenschilling, 1977; Nakagawa et al., 1986).

Initial conditions of dust disc and grain size

The temperature profile of the dust disc is same as disc described in section 2.3.1. The initial surface density profile is given by:

$$\Sigma(r) = 5.44 \cdot 10^{-3} \left(\frac{r}{100\ \rm au}\right)^{-1}\ \rm gr\ cm^{-2}. \tag{2.23}$$

I chose the grain size for which the particles have a Stokes number close to unity. For the parameters considered in section 2.3.1 for the gas disc, this size corresponds to $s_{\rm grain} = 1$ mm. The reason for that choice, is that I wish to study the particles that:

i) Feel the strongest radial drift.

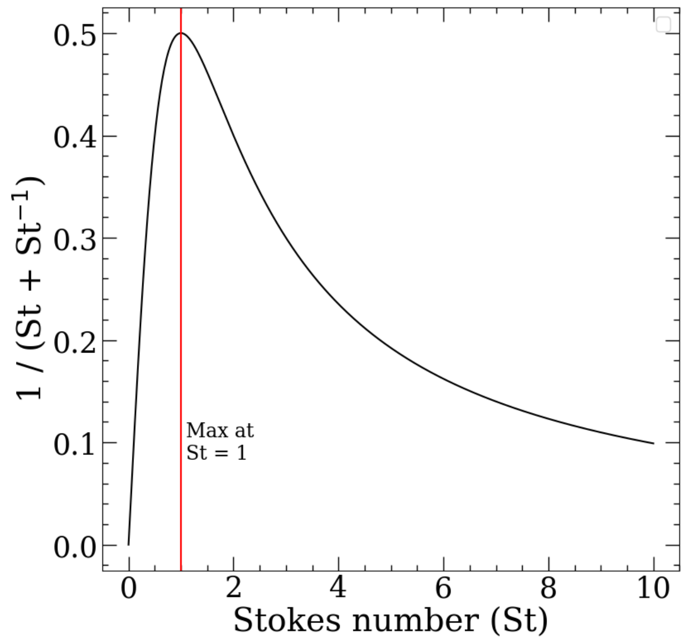

Figure 2.1: Function view $f(\mathrm{St}) = \frac{1}{\mathrm{St}+\mathrm{St}^{-1}}$. The maximum value is located at St = 1 (red line).

ii) Concentrate the most efficiently in the pressure maxima of the CBD.

Therefore, the millimetric dust will react efficiently to the gas structures and changes of local pressure of the gas. Consequently, the dust morphology will strongly depend on the binary parameters which affect the gas morphology.

Modification of the stopping time computation

The Equation (2.15) shows the dust is pressure-less fluid. Therefore, dust particles approach too much among them, and the smoothing length employed to compute the local dust density becomes very small. It triggers that the time step decreases significantly, and more iterations are required to compute the stopping time – this renders the computational cost prohibitively high. Then, for computational convenience, I modified the treatment, in which PHANTOM computes the stopping time.

In order to avoid this dust problem, I drop the ρ_d term and use instead $\rho_\mathrm{total} = \rho_g$ (in Equation (2.18)). By doing so, the stopping time is overestimated. This change only modifies the stopping time computation, and the K term in Equations (2.14) and (2.15), the equations that involve ρ_{g} and ρ_{d} mentioned in previous sections remain unchanged.

The stopping time is affected as:

$$\frac{t_{\mathrm{s,mod}}}{t_{\mathrm{s}}} = 1 + \epsilon, \tag{2.24}$$

where ϵ is the dust-to-gas ratio. The value of ϵ remains always below unity in all my simulations. Therefore, despite using this approximation, I obtain meaningful results for the dust evolution in the disc (at least for the short evolutionary times considered). A sanity check is discussed in Chapter 3.3 in order to confirm that the stopping time approximation, does not affect the results of this work.

2.4 Set of simulations

I carry out fourteen simulation, with the same disc parameters, but with different values of the binary inclination and eccentricity. The simulations are divided into two sets according to their eccentricity: $e_{\mathrm{B}} = 0.50$ and $e_{\mathrm{B}} = 0.75$. For each set, the inclinations are divided in prograde cases with $i_{\mathrm{B}} = \{0°, 30°, 60°\}$, the polar case with $i_{\mathrm{B}} = 90°$, and the retrograde cases with $i_{\mathrm{B}} = \{120°, 150°, 180°\}$. The names of the simulations are listed in Table 2.1. In Figure 2.2, I show the binary eccentricity and orientation with respect to the circumbinary disc. In the following, the disc is always seen face-on with the binary inclined inside the inner disc cavity.

Orbit name	e_{B}	i_{B}
$e50$-$i0$	0.50	0°
$e50$-$i30$	0.50	30°
$e50$-$i60$	0.50	60°
$e50$-$i90$	0.50	90°
$e50$-$i120$	0.50	120°
$e50$-$i150$	0.50	150°
$e50$-$i180$	0.50	180°
$e75$-$i0$	0.75	0°
$e75$-$i30$	0.75	30°
$e75$-$i60$	0.75	60°
$e75$-$i90$	0.75	90°
$e75$-$i120$	0.75	120°
$e75$-$i150$	0.75	150°
$e75$-$i180$	0.75	180°

Table 2.1: List of orbital parameters for each simulation. The parameters are the orbit name, eccentricity e_{B}, and inclination with respect to the disc i_{B}.

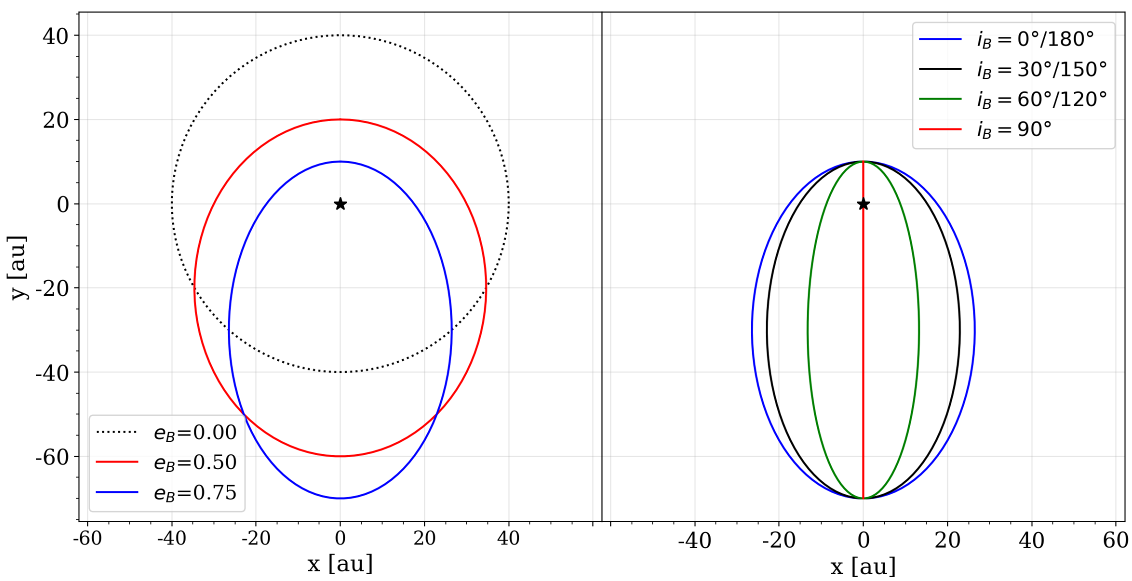

Figure 2.2: Parameter space of orbits modelled. The left panel shows face-on views of the two simulated eccentricities, $e_{\mathrm{B}} = 0.50$ in red and $e_{\mathrm{B}} = 0.75$ in blue. A circular orbit is shown with a dotted line for comparison. The right panel shows the projection of the orbit with $e_{\mathrm{B}} = 0.75$ for all seven modeled inclinations.

Chapter 3

Circumbinary disc simulations

Figures 3.1 and 3.2 show the gas and dust surface density maps — along with the dust-to-gas ratio — for $e_{\mathrm{B}} = 0.50$ and $e_{\mathrm{B}} = 0.75$ (respectively). The CBD is shown after 50 binary orbits. At this evolutionary stage, the structures in the dust distribution have reached a quasi steady-state.

We observe features of different kind in the CBD. A *horseshoe*, defined as the main gas over-density at the edge of the disc cavity. A *dust ring* along the disc inner edge, caused by the radial drift of the dust particles. When the horseshoe traps most of the dust, a *large clump* of dust forms on top of it. We also observe that the dust can also get trapped in other regions along the dust ring. Remarkably, these *small clumps* are not bound to the horseshoe. In the following, I describe each of these disc features: as a function of i_{B} (Sect. 3.1) and e_{B} (Sect. 3.2).

3.1 From prograde to retrograde cases

Prograde cases: the most striking structure observed in Figures 3.1 and 3.2 is the horseshoe at the inner edge of the disc. This is seen only at inclinations $i_{\mathrm{B}} = \{0°, 30°\}$, and for both eccentricities. This has already been reported in previous works of coplanar black hole binaries (Shi et al., 2012; D'Orazio et al., 2013; Farris et al., 2014) and stellar binaries (Ragusa et al., 2017). In particular, in the latter the authors report a dust concentration at the location of the horseshoe. This structure is comparable to the large dust clump observed in $e50$-$i0$, $e50$-$i30$, $e75$-$i0$, and $e75$-$i30$. However, I also observe the formation of small dust clumps outside the horseshoe. The differences between *large* and *small* clumps are their angular size and density. Quantitatively, the large clump is more than five times denser compared to the average dust density along the dusty ring; while the small clumps are only twice denser compared to the average value (see Figure 3.3). In addition, the large clump tends to overlap with the horseshoe covering roughly 60° in azimuth; while small clumps cover smaller azimuthal sectors (less than 30°). Remarkably, for $i_{\mathrm{B}} = 60°$, both the horseshoe and the large clump disappear. Instead, several small clumps appear along the dust ring. When this happens, the binary-triggered spirals and streamers are the only structures observed in the gas.

The cases with $i_{\mathrm{B}} = \{0°, 30°\}$ show an annular-shaped feature just outside the dense inner dust ring. This is easily seen in the dust-to-gas ratio maps of Figures 3.1 and 3.2. This structure forms due to the action of the gaseous spiral arms on the dust, which modifies the gas density in that region — and hence the Stokes number. This speeds up the radial velocity of the dust particles, which eventually leads to the formation of a dusty gap in the disc.

Polar configuration: for $i_{\mathrm{B}} = 90°$, We observe a set of 5 small clumps evenly distributed along the dust ring (Figure 3.3). The density of each of these clumps is about twice the average density of the dust ring.

Retrograde cases: in this configuration, We observe a remarkable difference between $e_{\mathrm{B}} = 0.5$ and $e_{\mathrm{B}} = 0.75$, as explained in Chapter 3.2. Nevertheless, a common aspect is that the densest gas regions are displaced toward the companion's orbital apoastron. This is shown in the bottom rows of Figures 3.1 and 3.2. The location of the densest region can be explained by the binary perturbations on the gas disc: the secondary star acts braking the surrounding gas. The deceleration is higher in the disc region closer to the companion (Nixon et al., 2011).

Additionally, It is important to notice that the cavity size decreases with increasing binary inclination as found by Miranda & Lai (2015). For instance, this effect can be easily seen by considering the shape of the dust ring. In addition, the cavity becomes eccentric and its centre does not match with the centre of mass of the system (Dunhill et al., 2015). The coplanar cases ($i_{\mathrm{B}} = 0°$) present cavity sizes in agreement with the classic result of (Artymowicz & Lubow, 1994) for different eccentricities.

Comparable values are observed in the dust-to-gas ratio ($\epsilon = \rho_{\mathrm{d}}/\rho_{\mathrm{g}}$) in the large and small clumps. This is because for the large clump, the dust and gas densities are high; while for the small clump both densities are lower. The implications of the high dust-to-gas ratio values will be discussed in Chapter 4.3.

Finally, we observe the formation of a circumprimary disc for $i_{\mathrm{B}} = 120°$ and $i_{\mathrm{B}} = 150°$. These kind of discs are likely transient and are hardly seen at this numerical resolution. This is because the low density of particles inside the cavity translates into a high numerical viscosity. Therefore, the circumstellar discs quickly drain into the stars, which are modelled as sink particles (see Chapter 2.2) as in Price et al. (2018b). These however, does not mean that circumstellar discs cannot form in such systems.

3.2 Eccentricity 0.50 versus 0.75

I find that the disc cavities are larger for $e_{\mathrm{B}} = 0.75$ compared to $e_{\mathrm{B}} = 0.5$, for the same inclination. This is in agreement with Miranda & Lai (2015). Also, the higher the binary eccentricity, the higher the density of the gas spirals and streamers. This is well seen for regrades cases with $e_{\mathrm{B}} = 0.75$: the gas disc exhibits both prominent spiral structures and multiple spiral arms. The latter are concentrated in a specific azimuthal sector of the CBD. These disc features are not observed for $e_{\mathrm{B}} \leq 0.50$, neither for coplanar configurations as in Ragusa et al. (2017). In Chapter 4, I show why the small dust clumps only form in retrograde configurations for $e_{\mathrm{B}} = 0.75$.

3.3 Numerical tests for small clump formation

In order to test whether or not the small dusty clumps reported in this work were caused by numerical effects, I performed a convergence test for different resolutions in dust. This was done for the case $e50$-$i90$ (i.e. my more representative example) at three

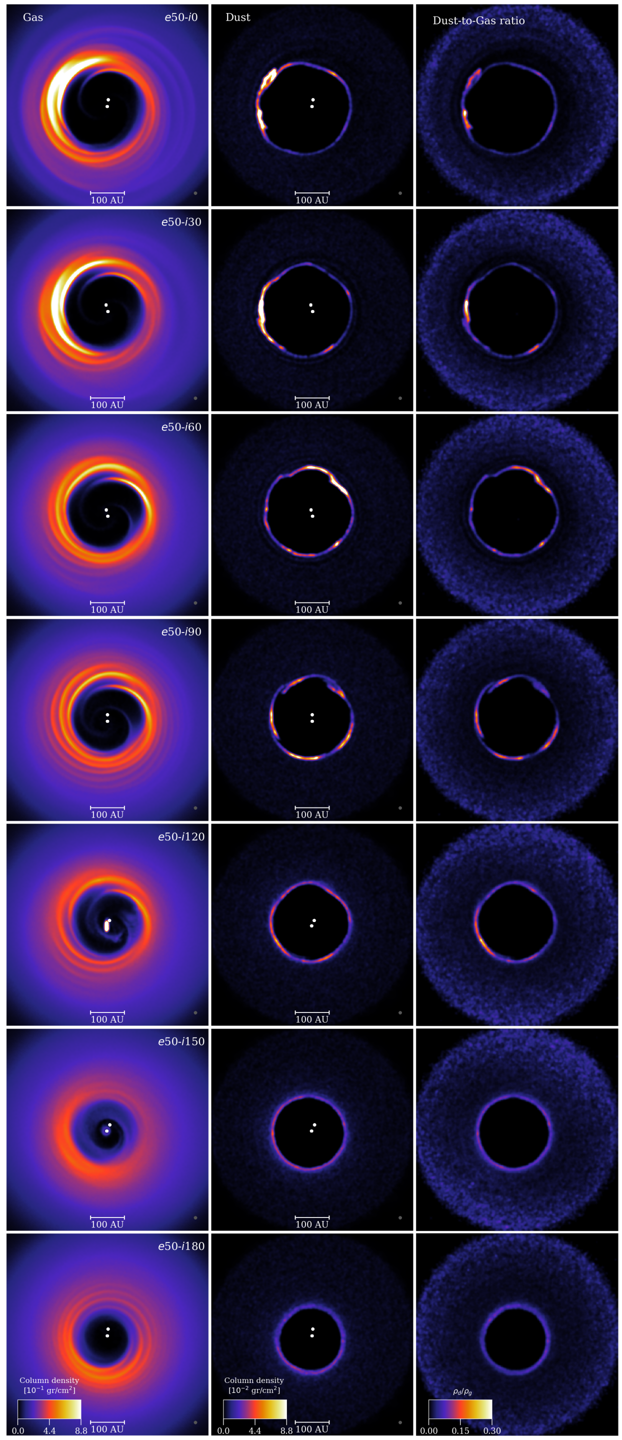

Figure 3.1: Gas (first column), dust (middle column) surface density in gr/cm^2 and the dust-to-gas ratio in last column, after 50 binary orbits at $e_\mathrm{B} = 0.50$. From upper to bottom are the different inclinations, $i_\mathrm{B} = \{0°, 30°, 60°, 90°, 120°, 150°, 180°\}$ respectively. The gray circle on the bottom-right corner of the two first columns represents the Gaussian kernel (5 au in diameter) used to smooth the images. This size is consistent with the highest ALMA angular resolution reached so far. I recall that in our simulations the physical quantities are computed using the smoothing length.

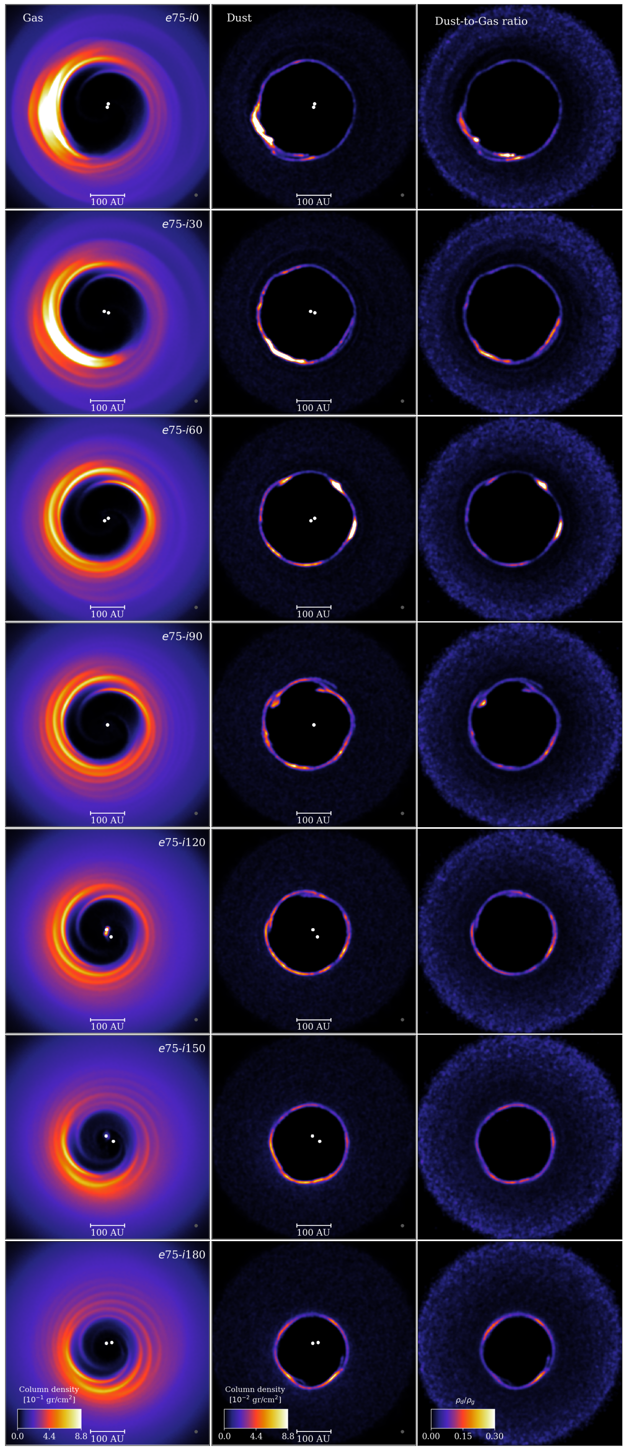

Figure 3.2: Same as Figure 3.1, but for the case $e_{\mathrm{B}} = 0.75$.

resolutions: $1.25 \cdot 10^4$, 10^5 (this work), and $4 \cdot 10^5$ dust particles; keeping the gas resolution fixed to 10^6 particles. These three simulations are shown in the left, middle, and right panels of Figure 3.4 (respectively). I observe that the low and high resolution tests exhibit the same structures (dust ring plus small clumps) as the simulation with 10^5 dust particles. Their azimuthal positions are identical for the resolutions considered. I also see that the proposed mechanism to form small clumps by bending the dust ring (see Chapter 4.1) still holds — regardless of the number of dust particles. The five clumps seen in Figure. 3.1 do not appear here because of the earlier evolutionary stage of the disc (11 binary orbits[1] instead of 50). Since I observe emergent small clumps, it is reasonable to expect these features to appear eventually. Based on these results, I thus conclude that the formation of small dusty clumps is a physical process, which is properly captured at the resolution of 10^5 dust particles.

Finally, in order to test whether the formation of small dusty clumps is affected by our approximation of the Stokes number (see Equation (2.19)) I performed a shorter simulation without the approximation, i.e., computing $\mathrm{St} \propto \rho_T^{-1} = (\rho_\mathrm{g} + \rho_\mathrm{d})^{-1}$. I did this for $e50$-$i60$ because it is the case that shows the highest dust-to-gas ratio values. Hence, it presents the most significant difference between the Stokes number computed with and without the approximation. Figure 3.5 shows the azimuthal density profile of both models. I see that regardless of the way the Stokes number is computed, the small clumps form, and at approximately the same azimuthal position. I therefore conclude that the approximation does not affect our results in any significant way.

3.4 Planetary companion in the polar case

To test whether the structures I found in the dust disc can also be triggered by planetary-mass companions, I performed two simulations with the very same setup as $e50$-$i90$, but with a companion mass of 10 M_J. In addition, I considered different values for the initial disc inner edge: $R_\mathrm{in} = 90$ au and $R_\mathrm{in} = 60$ au. Given the reduced strength of the gravitational perturbations, the reduced cavity size allows us to bring material closer

[1]This for the high computational cost discussed in section 2.3.2

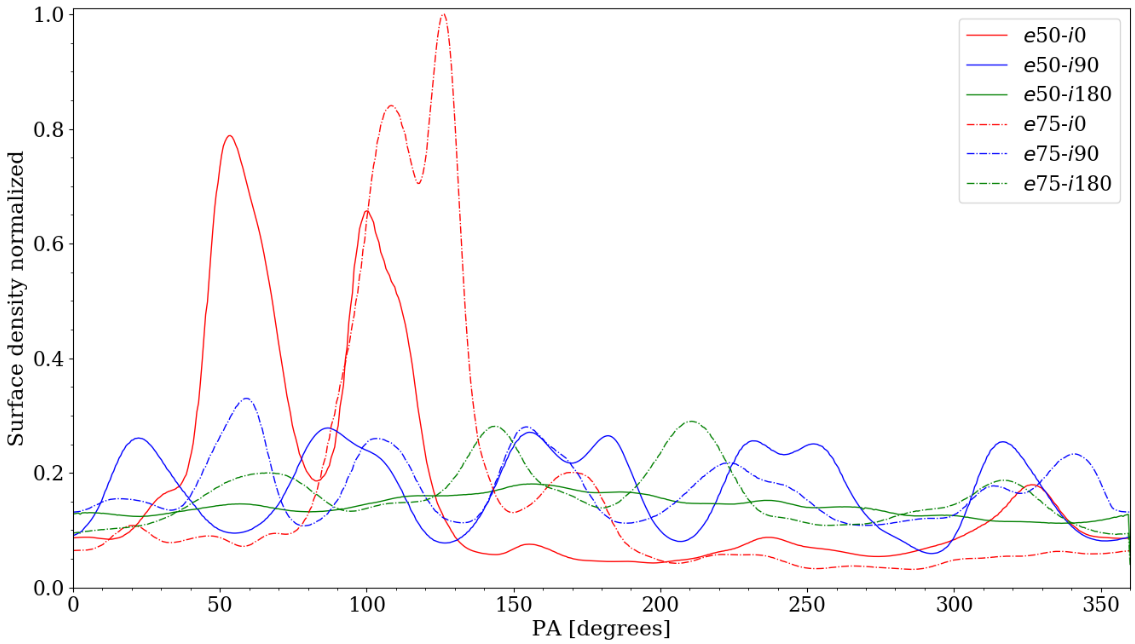

Figure 3.3: Normalised dust surface density along the dust ring. Prograde ($i_{\rm B} = 0°$), polar ($i_{\rm B} = 90°$) and retrograde ($i_{\rm B} = 180°$) cases are shown in red, blue, and green (respectively). Solid and dashed lines correspond to $e_{\rm B} = 0.50$ and $e_{\rm B} = 0.75$, respectively.

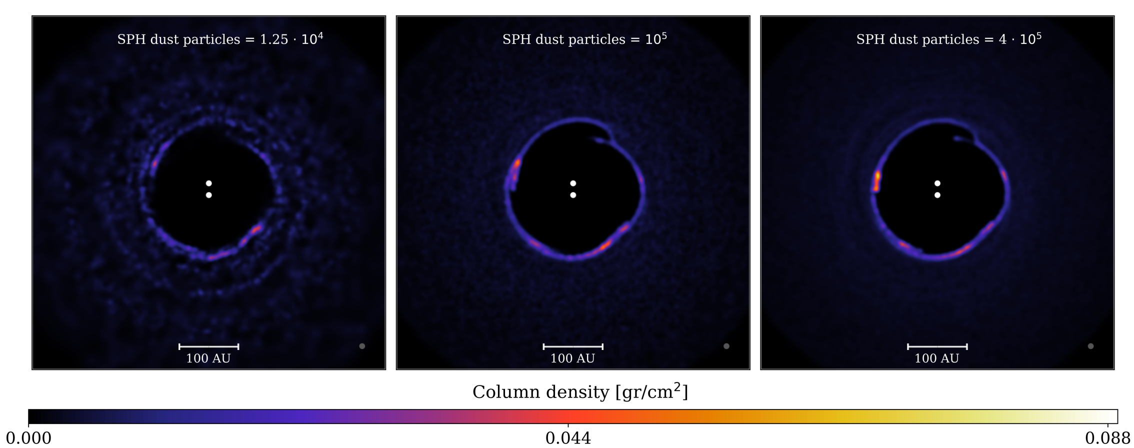

Figure 3.4: Dust distribution for the case $e50$-$i90$ after 11 binary orbital periods for different resolutions in dust: $1.25 \cdot 10^4$ (left), 10^5 (middle), and $4 \cdot 10^5$ (right) SPH dust particles. The gas resolution is fixed to 10^6 SPH gas particles for all the simulations. The formation of dusty clumps is not affected by the dust resolution.

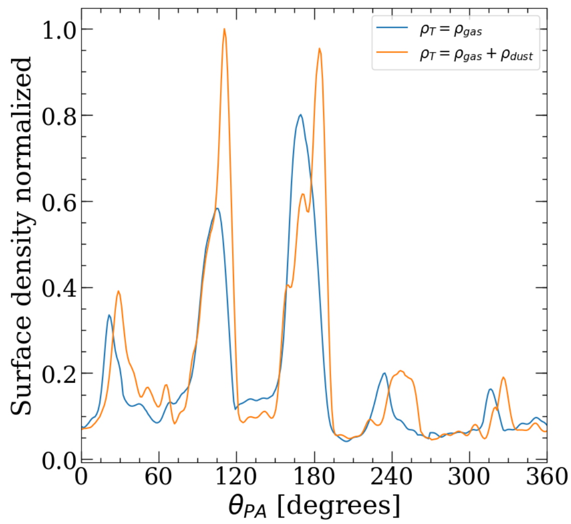

Figure 3.5: Azimuthal density profile along the dust ring after 21 binary orbits. The blue line corresponds to $e50$-$i60$ with the Stokes number computed with the approximation (St $\propto \rho_{\rm g}^{-1}$). Instead, the orange line corresponds to $e50$-$i60$ without the approximation (St $\propto (\rho_{\rm g} + \rho_{\rm d})^{-1}$, where ρ_g and ρ_d are the gas and dust density respectively).

to the inner planetary companion. In Figure 3.6, I show the dust and gas distributions after 50 planetary orbits. Regardless of the value of $R_{\rm in}$, the structures are different from the ones obtained for a stellar companion (see middle row in Figure 3.1). The only remarkable feature is the smooth dust ring. No small clumps nor spirals are observed. In summary, the latter features can only be triggered by a stellar companion for the configuration considered. This suggest that there is a mass threshold, which remains to be studied in detail.

3.5 Disc vertical scale-height at different radial distances

In Figure 3.7 I show $< h > /H$ for our simulations with $e_{\rm B} = 0.5$ (left panel) and with $e_{\rm B} = 0.75$ (right panel). Since $< h > /H < 1$, the disc is properly resolved in the vertical direction. The value of the Shakura–Sunyaev viscosity $\alpha_{\rm SS}$ can be easily inferred from the values of $< h > /H$ in Figure 3.7. In this case, it is of the order of 0.005 as mentioned in the text and as in the simulations in Price et al. (2018b).

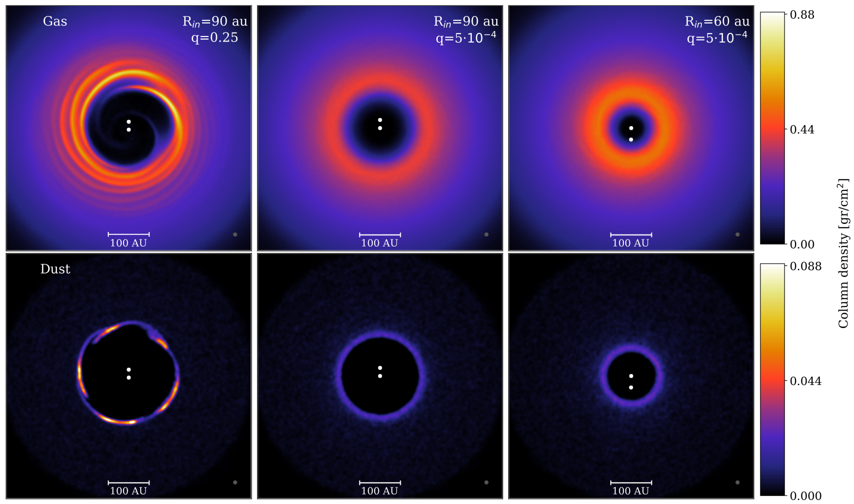

Figure 3.6: Gas (top panels) and dust (bottom panels) morphology for the case $e50$-$i90$ after 50 binary orbits (left panel), and a companion mass reduced to 10 $M_{\rm J}$ (i.e. 50 times less massive) with the same disc parameters of the case $e50$-$i90$. The initial disc inner edge is set at 90 au and 60 au in the middle and right panels, respectively. A planetary companion is not able to trigger the formation of dusty clumps in the disc.

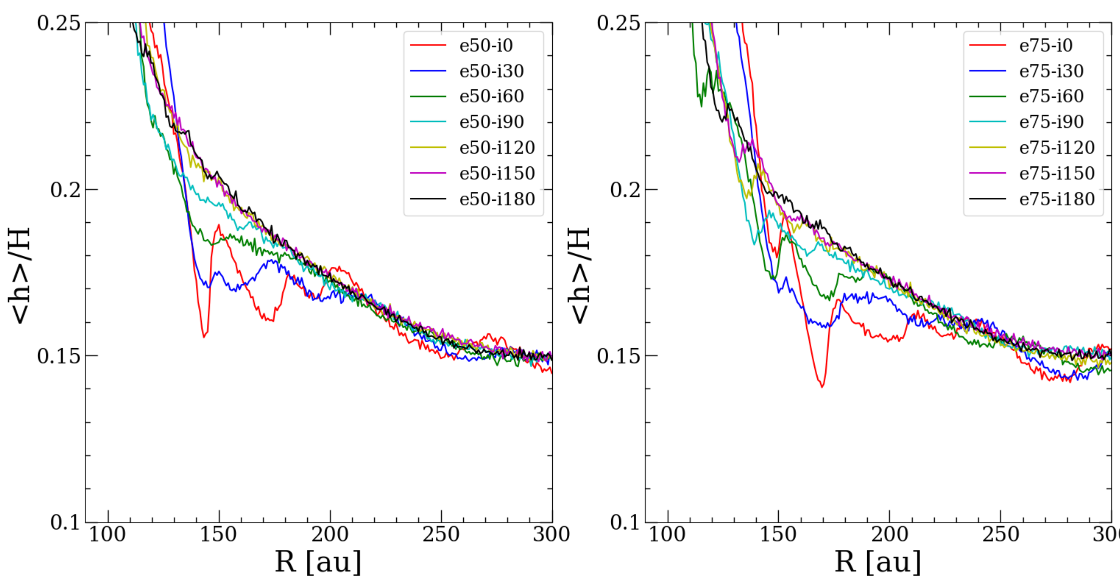

Figure 3.7: Radial profiles of $< h > /H$ after 50 binary orbits for all the simulations with $e_{\rm B}$ = 0.50 (left panel) and with $e_{\rm B} = 0.75$ (right panel).

Chapter 4

Dusty clump formation and evolution

As reported in Chapter 3, large and small clumps can form along the dust ring according to the binary parameters. The mechanism of dust trapping by a local azimuthal gas over-density — namely the horseshoe — has already been studied extensively in previous works (e.g., Johansen et al., 2004; Birnstiel et al., 2013; Owen & Kollmeier, 2017; Ragusa et al., 2017). However, to the best of our knowledge, the formation of small dust clumps in CBDs has not been reported yet. These features are particularly prominent for $i_{\rm B} = 90°$, but they also appear for $i_{\rm B} = \{0°, 30°\}$.

The main characteristic of the small clumps is that, although they form on top of local gas over-densities, they do not necessarily follow the gas. This is in contrast to the large clump, explained above. Below, I focus in more detail on the formation of small clumps.

4.1 Formation of a single small clump

For the coplanar retrograde ($i_{\rm B} = 180°$) case, small clumps are only observed for $e_{\rm B} = 0.75$ (as opposed to $e_{\rm B} = 0.50$). This is because a higher eccentricity favours the formation of more prominent gas spirals and denser streamers. These gaseous features caused by the inner binary are crucial to trigger the small clump formation. Specifically, the binary-induced gaseous streams perturb the dusty ring through aerodynamical drag.

The strength of the latter heavily depends on the Stokes number (see Equation (2.19)). For sake of simplicity, let's assume that the dust ring has a constant density, which is a reasonable approximation before any clump forms along the ring. Since the grain size is fixed, then the Stokes number only depends on the gas density.

The process of small clump formation is shown in Figure 4.1 where I schematically represent the motion of the dust on top of the gaseous spirals. The inner spiral (called the *head*) is caused by the companion, while the outer one (called the *tail*) corresponds to the spiral formed in the previous orbit. The *tail* is at a larger distance from the binary compared to the *head*. The dust ring (in red) is deformed by the two gaseous spirals. The Stokes number in both spirals is less than one due to their high gas density, whereas it is higher in the region between the two spirals. For our disc parameters, 1 mm grains have St $<<$ 1 in the spirals and St $\sim$ 1 in between. Due to the strong coupling, the inner dust ring follows the *head*, whereas the outer dust ring follows the *tail*. In addition, the bending of the dust ring generates a significant radial density gradient. As a consequence, the dust particles in between the spirals radially drift towards the *head*. This effect is the strongest for mm-sized grains because their Stokes number is close to one (Weidenschilling, 1977). Therefore, millimetric dust is efficiently accumulated at the *head* location, where a small clump begins to form.

4.2 Evolution and behaviour of a single small clump

Because of the periodic perturbation of the disc caused by the binary, gas spirals continuously form at a specific azimuthal sector of the disc. Therefore, after one binary orbit, the previous head becomes the tail (with a small clump attached to it) and the innermost gas stream becomes the head. This explains why dust clumps are periodically formed in the CBD in the simulations shown in Chapter 3.

Once the clumps form, there are two possible dynamical outcomes: they can either be disrupted or keep growing. The survival and long-term behaviour of these *individual structures* are key for grain growth, and consequently for planetesimal formation in the disc. The survival of the small clumps is related to the local Stokes number.

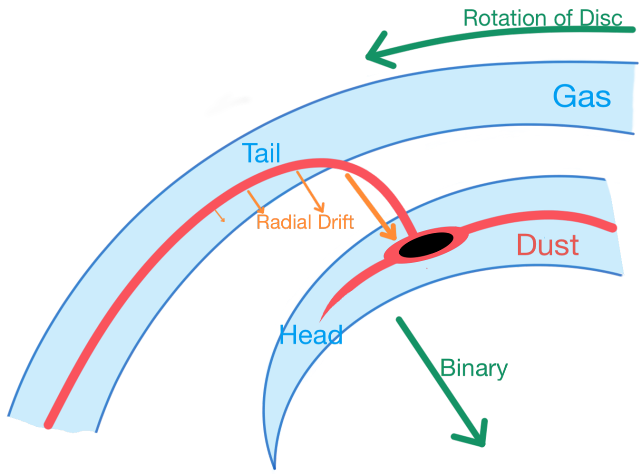

Figure 4.1: Sketch of the mechanism of formation of a small clump. The gaseous spirals are represented in blue and the dust ring in red. The forming small clump is highlighted in black. The disc rotation and the binary centre of mass location are shown with green arrows. The length of the orange arrows indicates the magnitude of radial drift, which is higher in the region between the spirals.

The region where gaseous spirals are formed has high density – clumps will have Stokes numbers less than one in there. Therefore, even though the small clump formation happens in that region, the clump can also be easily stretched and potentially disrupted. Such stretching is caused by the gradient of angular velocity within the clump due to interaction between the clump and the spiral. More specifically, the head of the spiral moves faster compared to the regions behind it. To characterise the evolution of the small clumps, I define their corresponding survival timescale as the time from their formation until their disruption. In all my simulations, I observe survival timescales of at least one orbital period at the clump radial distance. It is precisely when the clump completes the first orbit and returns to the spiral-forming region that it can be potentially disrupted. I also note that the inclination affects the clump survival time. For instance, in cases with $i_{\rm B} = 90°$, the binary torque does not strongly affect the azimuthal velocity gradient of the gas spiral. In this configuration, the small clumps survive for several tens of orbits.

Besides disruption, the clump can also be fed after completing an orbit. Figure 4.2 shows all the possible scenarios that a small clump can experience. The first one, called

A, happens when a dust stream falls exactly onto the small clump, making it grow. The other three scenarios (B, C, and D) lead to clump disruption. Once the small clump is disrupted, its remnants are later fed by the outer dust stream. However, it is worth noting that the previous clump never reforms as such. To sum up, it is possible to either generate a more massive clump (A); or to disrupt the main clump generating several ones (B, C, and D).

Throughout all the simulation, the circumbinary disc is periodically perturbed by the companion. This ensures the continuous formation of clumps as previously described. At the end of our simulations (i.e. after 100 binary orbits) the dust disc exhibits a similar morphology as the one observed after 50 binary orbits. Nevertheless, it is worth noting that the individual small clumps shown at 50 orbits are not necessarily the same as the ones present at the end of the simulation.

4.3 Dust-to-gas ratio

Interestingly, if the dust-to-gas ratio becomes close to one then self-induced dust traps (Gonzalez et al., 2017) could appear in the disc. The increase of the dust-to-gas ratio could also potentially trigger the streaming instability (Johansen & Youdin, 2007). Therefore these could be *sweet spots* for grain growth and planetesimal formation in the CBD. However, these dynamical effects are not seen in our simulations due to their short evolutionary time. In addition, SPH is not the most suitable method to capture streaming instability effects due to the two-fluid numerical scheme (Laibe & Price, 2012a). I did not run the models for longer, as the density approximation described in section 2.3.2, namely $\rho = \rho_{\rm g}$, becomes less valid precisely as the dust-to-gas ratio increases.

4.4 Clumps formation with different grain sizes

So far, I have only discussed the large and small clump formation for one specific grain size, namely mm-sized particles. Here, I present simulations with two other grain sizes: 100 μm and 1 cm. Figures 4.3 and 4.4 show the dust morphology for $e50$-$i0$ and $e50$-$i90$, respectively. In addition, I also show a test simulation without aerodynamic drag (labelled

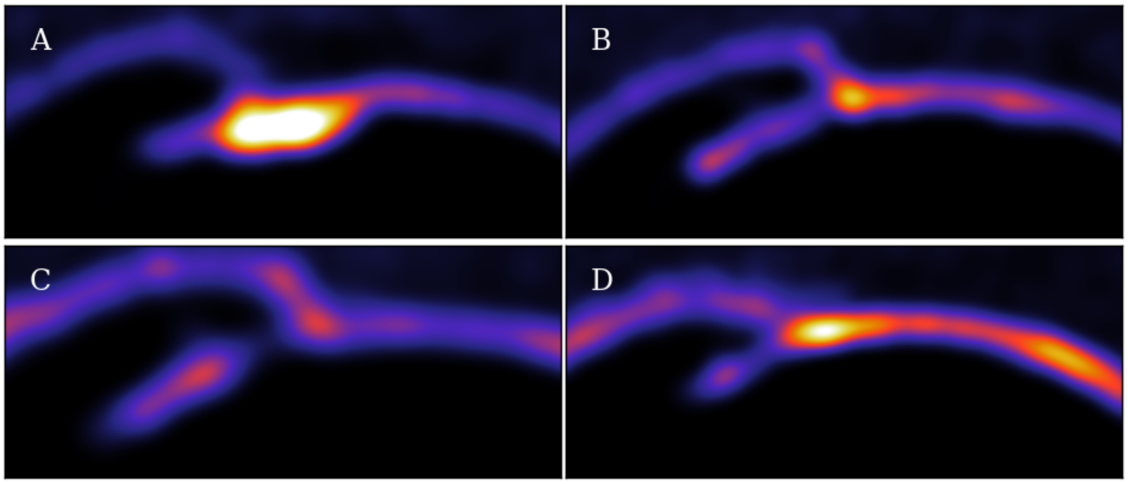

Figure 4.2: The four possible scenarios that can experience a small clump after its formation. These examples are taken from the simulation $e50$-$i90$ at different times. In A, the clump is fed by a dust stream, without being disrupted. In B, I see a third clump forming in between a disrupted clump. In C and D, the dust streams feeds the back and front side (respectively) of a disrupted clump.

"no drag"), where the dust particles behave as test particles.

Comparing Figures 4.3 and 4.4, we observe that the grain size plays a crucial role in the formation of clumps. This is because the dust coupling (i.e. the Stokes number) depends linearly on the grain size for the Epstein regime, as shown in Equation (2.19). In particular, the proposed formation mechanism (see Chapter 4.1) is the most efficient for dust grains with a Stokes number varying from one to slightly less than one along the orbit, which corresponds to 1 mm for the chosen disc parameters. Nevertheless, for other disc parameters (e.g. disc mass, temperature and density profiles, etc.), the condition St ~ 1 would correspond to a different grain size, which would form structures similar to the ones reported here.

Interestingly, the dust ring and the clumps are mainly caused by gas drag effects, and not only by the binary gravitational perturbations. For instance, in the no-drag simulations it is not observed any clumps or dusty rings along the cavity.

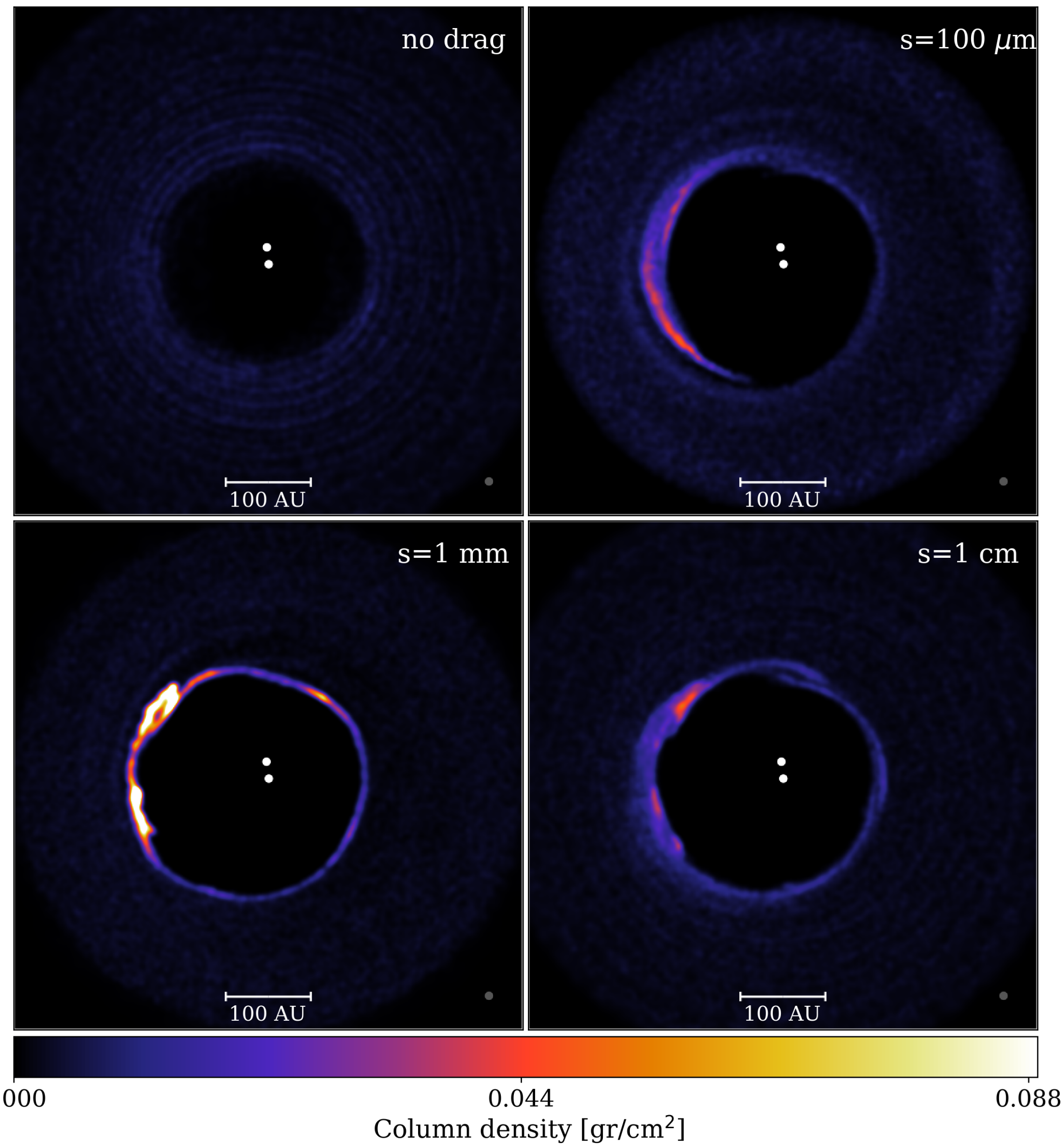

Figure 4.3: Dust distribution of the case $e50$-$i0$ after 50 initial binary orbits, for three sizes of dust grains, plus one simulation without the aerodynamic drag. The dust grain sizes are 100 microns, 1 millimetre, and 1 centimetre. The no-drag simulation was made for $s = 1$ mm.

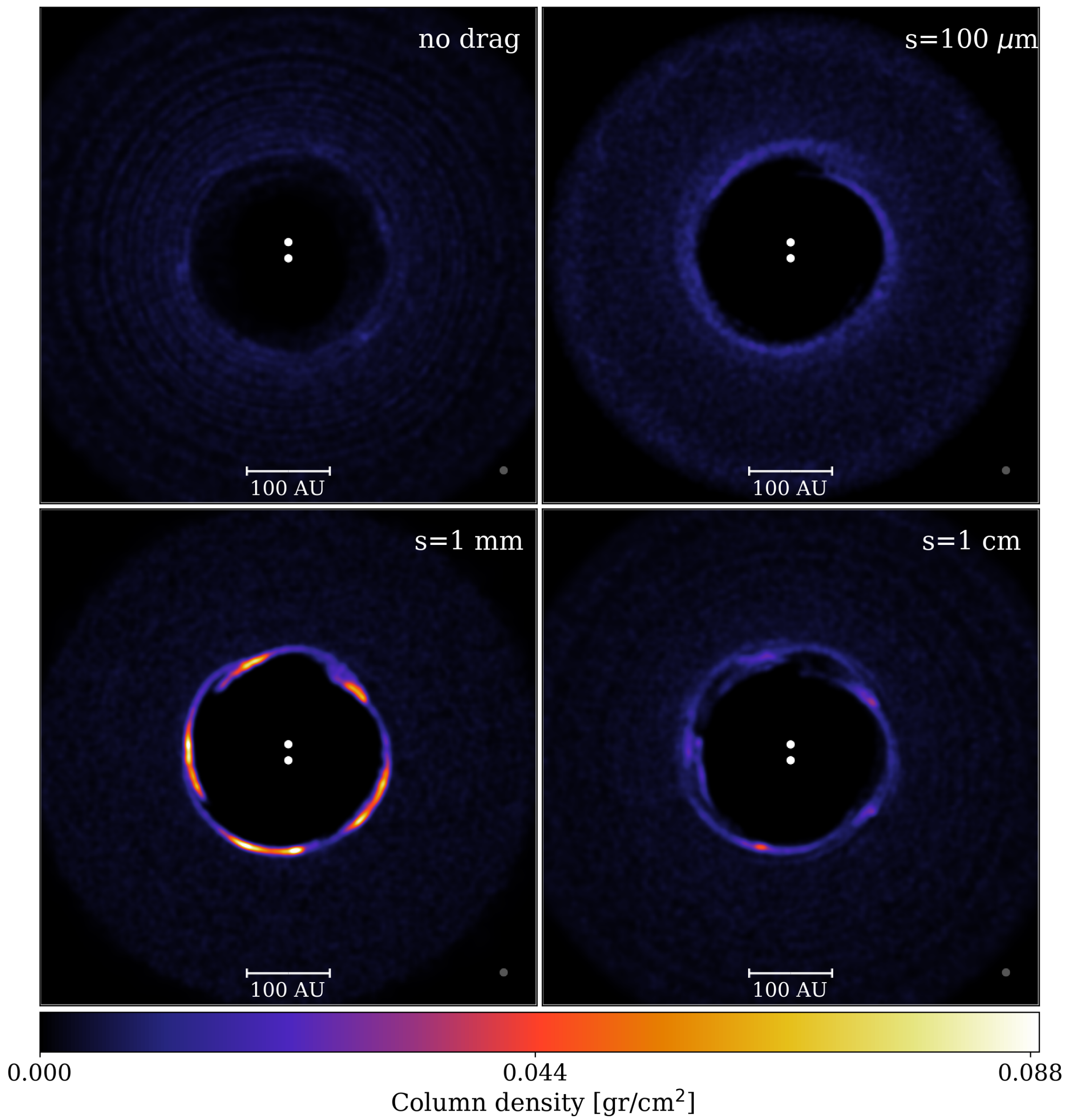

Figure 4.4: Same as Figure 4.3, but for the case $e50$-$i90$.

Chapter 5

Dust features as indicators of unseen stellar companion

Direct observations of stellar companions in binary systems are particularly challenging. Specifically, there are strong limitations to properly resolve the separation between two stars. This is even worse if the companion is less massive and therefore fainter compared to the main star. However, here I have shown that some prominent disc features can be triggered by the gravitational interaction of a low-mass stellar companion inside the cavity. More specifically, the set of simulations of this work explore a modest but meaningful region of the vast space of parameters, namely the binary eccentricity and inclination. Hence, in principle, the disc features could be used to infer the orbit of a potentially unseen stellar companion.

5.1 Remarkable dust structures in CBDs

- *Large dusty clump within a gas horseshoe.* These features appear in all our simulations with $i_{\rm B} \leq 30°$. Both have the same properties as the ones reported by Ragusa et al. (2017). They are not produced by a vortex, and have a high contrast compared to the rest of the disc. Thus, a large dusty clump on top of a gas horseshoe could be an indicator of an inner companion with an orientation close to the disc plane.

- *Embedded small clumps in a dusty ring.* For all our highly-inclined simulations ($60^\circ \leq i_\mathrm{B} \leq 120^\circ$), we observe several small dusty clumps embedded in the disc. Interestingly, in the polar case, clumps are azimuthally equidistant between them. Therefore, several small clumps along the dust ring could indicate the presence of a *highly inclined* inner companion. Note that the case $e75$-$i180$ shows a clumps structure too, therefore a highly eccentric and retrograde companion is also able to create the same feature. In Chapter 3.4 I showed that an inner planet-mass companion does not produce such structures, which suggests the existence of a mass threshold for structure formation in the CBD.

- *Smooth dust ring.* All the cases that do not show any remarkable features (horseshoe or clumps) in the dust ring are included in this category. In the absence of structure it is hard to draw any conclusion on whether there is a single star or a binary system. Nevertheless, the inner cavity structure could help to infer the presence of an inner companion. For instance, during the early disc evolution, a large inner cavity of several tens of au strongly suggests the presence of a binary system inside the cavity. However, for more evolved discs and if no accretion is detected, the cavity is more likely to be caused by photoevaporative processes (Alexander et al., 2006; Owen, 2016)

Caution is required when interpreting my results since this analysis mainly applies to grains with a Stokes number close to unity. See for instance the structures obtained for different grain sizes in Figures 4.3 and 4.4. HD 142527 is a notorious example where two different dust structures coexist: a large clump at millimetric wavelengths (Boehler et al., 2018) and small clumps at centimetric wavelengths (Casassus et al., 2015b).

When spirals are observed, their morphology and their azimuthal concentration in particular can provide further information on their dynamical origin. Besides an inner binary, flybys (Cuello et al., 2019a), planets (Dong et al., 2015), self-gravitating discs (Dipierro et al., 2015a; Forgan et al., 2018), or shadows (Montesinos et al., 2016; Montesinos & Cuello, 2018; Cuello et al., 2019b) can also produce spiral arms in the disc. The main difference is that the spirals caused by an eccentric inner companion are often multiple and well concentrated in one azimuthal sector of the disc, as opposed to the other mechanisms.

5.2 The AB Aurigae system

AB Aurigae – an Herbig Ae star of the A0 spectral type and mass $2.4 \pm 0.2\ M_{\odot}$ (DeWarf et al., 2003) – exhibits a very complex morphology, both in gas and dust: i) multiple spiral arms in scattered light (Fukagawa et al., 2004; Corder et al., 2005; Hashimoto et al., 2011), ii) a horseshoe-shaped dust trap (Tang et al., 2012; Pacheco-Vázquez et al., 2016), iii) and a large dust cavity at a distance from the star between ~ 70 and 100 au (Hashimoto et al., 2011; Tang et al., 2012). A single planet has been proposed to explain some of the observed features (Hashimoto et al., 2011; Fuente et al., 2017; Tang et al., 2017). Tang et al. (2012) were only able to explain the cavity size by adding a body at $r \sim 45$ au and $M = 0.03 M_{\odot}$; whereas Fuente et al. (2017) managed to explain the emission of the dust disc by putting a Jupiter-mass planet at $r = 94$ au. It is however challenging to explain all the aforementioned features simultaneously.

Instead, the binary scenario proposed by Price et al. (2018b) for HD 142527 seems more promising. As a matter of fact, there is a striking similarity between the structures observed in AB Aurigae and those in HD 142527. Pirzkal et al. (1997) gives an upper limit of $0.25\ M_{\odot}$ down to 60 au for an possible inner stellar companion in AB Aurigae. It is worth noting that mass constraint at small radii is difficult to quantify, the mass upper limit could be greater. Therefore, a low mass ratio binary scenario for AB Aurigae is reasonable. Based on the disc observations, our models suggest the presence of an inner stellar companion — undetected so far.

As mentioned in Chapter 5.1, the absence of a gas horseshoe and the multiple spiral arms suggest a high eccentricity and an inclination higher than 30°. In particular, the case $e50$-$i60$ reproduces the observed dust distribution remarkably well (see Figure 5.1), simultaneously explaining the multiple and azimuthally concentrated gaseous spirals in the disc (not shown). Figure 5.1 shows a comparison between the observed dust continuum emission at 1.3 mm (Tang et al., 2012) and the dust distribution in $e50$-$i60$, where the dust over-density is seen as a large clump due to beaming effects. In addition, Rivière-

Marichalar et al. (2019) very recently reported the observation of clumps in HCN – a good tracer of cold and dense gas – around the inner edge of the disc. This supports the idea that the dusty clumps might be real. It is worth to mention however that a bad coverage of the uv plane could produce artificial clumps in the reconstructed intensity map. Indeed, the 0.9 mm image presented by Tang et al. (2017) shows a continuous inner ring, rather than clumps (see Figure 5.2). Nevertheless, the same simulation with a grain size of 100 μm reproduces remarkably well the continuum emission. Future observations at a higher angular resolution and with better uv plane coverage are required in order to reveal whether *small clumps* are indeed embedded in the disc of AB Aurigae.

In summary, these results strongly motivate the search for a stellar companion within the cavity of the disc around AB Aurigae. More specifically, an i) unequal-mass, ii) eccentric, and iii) inclined stellar binary can potentially explain most (if not all) the observed disc features.

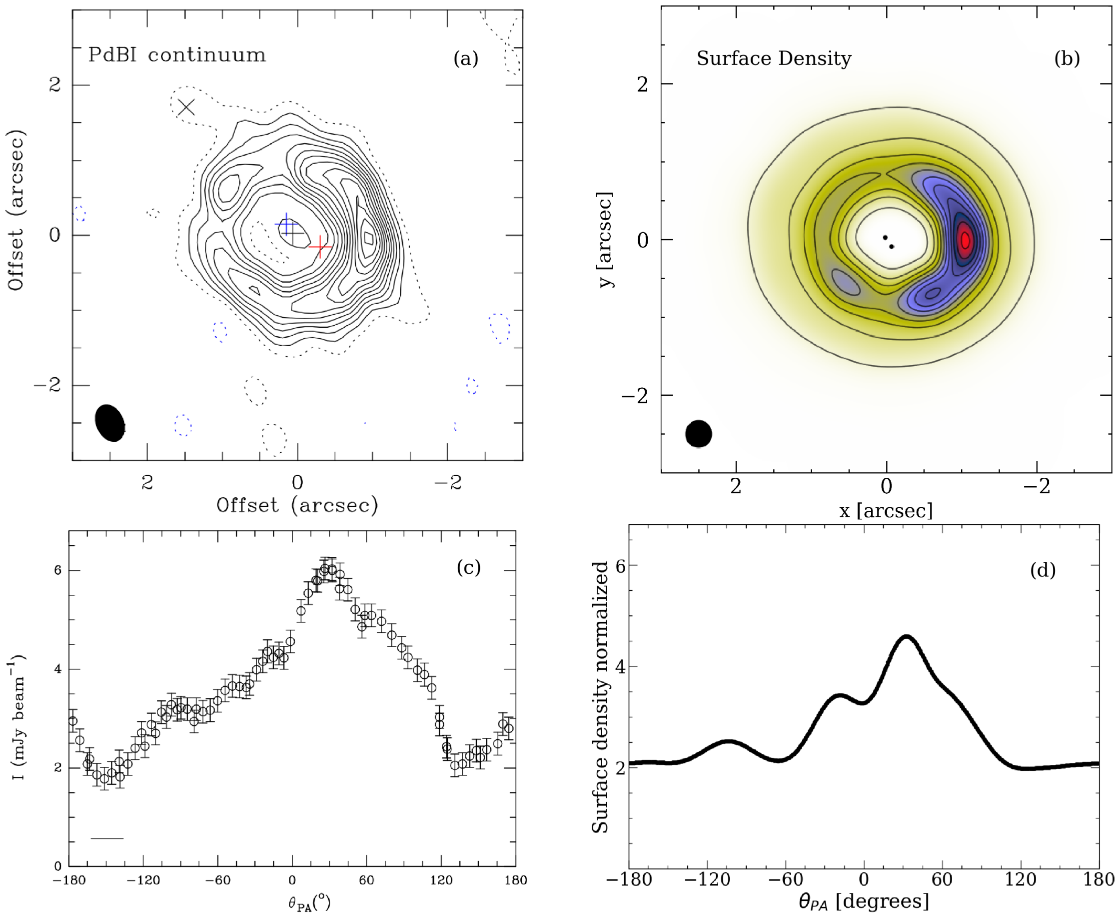

Figure 5.1: Comparison between the observation at 1.3 mm of AB Aurigae (left column) and the dust distribution in $e50$-$i60$ after 100 orbits (right column). **(a)**: Dust continuum emission at 1.3 mm. The black cross represents the stellar peak. The blue and red crosses mark the peak of ^{12}CO J=2→1: highest blue-shifted and red-shifted peak respectively. **(b)**: Surface density map from $e50$-$i60$ convolved by a 50 au beam (shown in the left corner), consistent with the observations in (a). **(c)**: 1.3 mm intensity along the dust ring. **(d)**: Surface density along the dust ring normalised to the average dusty ring density. The frame orientation is chosen so the dust over-density is roughly at the same azimuthal position as that in the the observation, and inclined $-23°$ with respect to the x-axis as the observed system Tang et al. (2012). The $\theta_{\rm PA}$ in **(c)** and **(d)** represents the offset of the PA position at 121.3°, measured from the north in a clockwise sense. The observations in (a) and (c) are taken from Figures 1 and 11 in Tang, A&A, 547, A84, 2012, reproduced with permission © ESO.

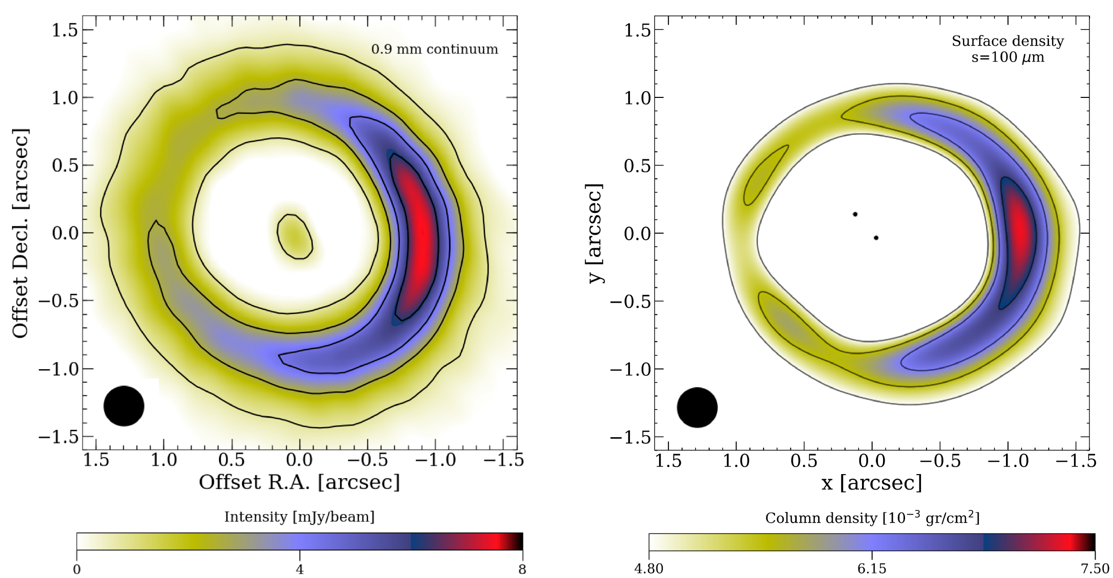

Figure 5.2: Comparison between the observation at 0.9 mm of AB Aurigae (left panel) and the dust distribution in $e50$-$i60$ for $s = 100$ μm (right panel).

Chapter 6

Conclusions

I performed 3D SPH gas and dust simulations of circumbinary discs (CBDs) around binaries with different eccentricities and inclinations. I considered unequal-mass binaries similar to HD 142527. This allowed us to characterise the disc morphology for different combinations of orbital parameters of the companion. The main conclusions of my work are the following:

1. An inner stellar companion with a low inclination ($i_{\rm B} \leq 30°$) with respect to the CBD is able to trigger a horseshoe-like structure in both the gas and the dust. Additionally, small dust clumps can also appear along the dusty ring. The latter had not been reported by previous works.

2. For an inner stellar companion on a highly inclined orbit with respect to the CBD ($60° \leq i_{\rm B} \leq 120°$) the dust ring breaks into small clumps, evenly distributed along the cavity.

3. For high eccentricities ($e_{\rm B} = 0.75$), the binary perturbations on the gas disc become stronger — especially for retrograde cases ($120° \leq i_{\rm B} \leq 180°$). This translates into denser gas structures: spirals, streams, and horseshoes. Therefore, the higher the eccentricity the easier the formation of clumps.

4. The small clump structure strongly depends on the Stokes number of the dusty ring. The formation mechanism is most efficient when the Stokes number is close to unity.

A detailed description of its formation and evolution is given in Chapter 4.

Circumbinary discs are often thought to be unfavourable systems for planetesimal formation, because of the high relative velocities expected among solid bodies (Bromley & Kenyon, 2015). In this work, I have found that high dust-to-gas ratio clumps form in the inner regions of discs around unequal-mass, eccentric, and inclined binaries (especially for polar configurations). Such clumps could then constitute *sweet spots* for dust accumulation and grain growth (Gonzalez et al., 2017; Owen & Kollmeier, 2017), suggesting that CBDs could potentially be efficient planetesimal cradles.

Within this context, polar circumbinary discs are of particular interest since I have shown they form stable and prominent dusty clumps ($e50$-$i90$ and $e75$-$i90$). Theoretical models first predicted the existence of this kind of polar discs (Aly et al., 2015; Martin & Lubow, 2017; Zanazzi & Lai, 2018; Lubow & Martin, 2018), as the one very recently discovered in HD 98800 by Kennedy et al. (2019). It seems reasonable to think that planets will eventually form in these polar circumbinary discs. Based on that assumption, Cuello & Giuppone (2019) showed that binaries with mild eccentricities are more likely to retain their circumbinary P-type polar planets (also known as *polar Tatooines*). In this regard, systems similar to $e50$-$i90$ are better candidates to host this type of polar planets.

Interestingly, the asymmetric disc features aforementioned can be much more easily detected than the binary itself. Considering the systems categorised as *Giant Discs* by Garufi et al. (2018), several of them show multiple, asymmetric, relatively faint arm-like structures on large scales. Based on our results, I am inclined to think that there might be binaries in the cavities of several of those discs. In particular, I strongly suggest the presence of an eccentric and inclined inner companion in AB Aurigae.

Future work

There are three aspects that are direct projections of this work.

1. Small clumps in the polar configuration: Probably the most interesting observed feature, of all simulations, is the five-small clumps system at the dusty ring for polar cases. The questions that remain are: why are they five? and why are they evenly distributed along the cavity? A possible explanation could come from linking the position of the dusty ring with the resonance modes of the binary. However, it will be necessary to make more simulations, and it will be essential to explore different masses and semi-major axis combinations to have a robust explanation.

2. Connect more features of the AB Aurigae system with a binary as $e50$-$i60$: The comparison between the observation of AB Aurigae (see Figure 5.1) with my simulations was made at the regions outside the cavity. And it reproduces very well the features observed there. Nevertheless, the system exhibits more enigmatic features inside the cavity. Namely two spirals arms in CO (Tang et al., 2017), complex kinematic (Tang et al., 2017; Rivière-Marichalar et al., 2019), twisted inner regions with respect to the protoplanetary disc (Hashimoto et al., 2011), and a bridge in HCO^+ emission that connects the inner disc rim with the central region (Rivière-Marichalar et al., 2019). The case $e50$-$i60$ looks very promising to explain some of these aspects, but it is necessary to make simulations that include radiative transfer models and to get a higher resolution in the cavity.

3. Explore the interesting resemblance between the HD 169142 system and the polar cases $e50$-$i90$ and $e75$-$i90$: Pérez et al. (2019) released a 1.3 mm ALMA observation of the HD 169142 system where, at the inner ring, they detect a dust morphology very similar to I showed for the polar case. Indeed, there is up to four small dusty clumps present in the disc. Therefore, new simulations and observations will be required to explore the presence of a possible stellar inner companion on a polar orbit (undetected so far).

Bibliography

ALMA Partnership et al., 2015, , 808, L3

Alexander R. D., Clarke C. J., Pringle J. E., 2006, , 369, 216

Aly H., Dehnen W., Nixon C., King A., 2015, , 449, 65

Andrews S. M., et al., 2018, , 869, L41

Armitage P. J., 2018, A Brief Overview of Planet Formation. p. 135, doi:10.1007/978-3-319-55333-7˙135

Artymowicz P., Lubow S. H., 1994, , 421, 651

Ataiee S., Pinilla P., Zsom A., Dullemond C. P., Dominik C., Ghanbari J., 2013, , 553, L3

Avenhaus H., Quanz S. P., Schmid H. M., Meyer M. R., Garufi A., Wolf S., Dominik C., 2014, ApJ, 781, 87

Avenhaus H., et al., 2018, , 863, 44

Bate M. R., Bonnell I. A., Price N. M., 1995, , 277, 362

Benisty M., et al., 2015, , 578, L6

Benisty M., et al., 2017, , 597, A42

Benisty M., et al., 2018, , 619, A171

Biller B., et al., 2012, , 753, L38

Birnstiel T., Dullemond C. P., Pinilla P., 2013, , 550, L8

Boehler Y., Weaver E., Isella A., Ricci L., Grady C., Carpenter J., Perez L., 2017, ApJ, 840, 60

Boehler Y., et al., 2018, , 853, 162

Bromley B. C., Kenyon S. J., 2015, , 806, 98

Casassus S., et al., 2013, , 493, 191

Casassus S., et al., 2015a, ApJ, 811, 92

Casassus S., et al., 2015b, ApJ, 812, 126

Casassus S., et al., 2018a, preprint, p. arXiv:1805.03023 (arXiv:1805.03023)

Casassus S., et al., 2018b, , 477, 5104

Cazzoletti P., et al., 2018, , 619, A161

Christiaens V., Casassus S., Perez S., van der Plas G., Ménard F., 2014, ApJL, 785, L12

Christiaens V., et al., 2018, , 617, A37

Claudi R., et al., 2019, , 622, A96

Corder S., Eisner J., Sargent A., 2005, , 622, L133

Cuello N., Giuppone C. A., 2019, arXiv e-prints, p. arXiv:1906.10579

Cuello N., et al., 2019a, , 483, 4114

Cuello N., Montesinos M., Stammler S. M., Louvet F., Cuadra J., 2019b, , 622, A43

D'Orazio D. J., Haiman Z., MacFadyen A., 2013, , 436, 2997

DeWarf L. E., Sepinsky J. F., Guinan E. F., Ribas I., Nadalin I., 2003, , 590, 357

Dipierro G., Pinilla P., Lodato G., Testi L., 2015a, , 451, 974

Dipierro G., Price D., Laibe G., Hirsh K., Cerioli A., Lodato G., 2015b, Monthly Notices of the Royal Astronomical Society: Letters, 453, L73

Dipierro G., Laibe G., Price D. J., Lodato G., 2016, Monthly Notices of the Royal Astronomical Society: Letters, 459, L1

Dipierro G., et al., 2018, , 475, 5296

Dong R., Zhu Z., Rafikov R. R., Stone J. M., 2015, , 809, L5

Dong R., et al., 2018, , 860, 124

Draine B. T., 2006, , 636, 1114

Duchêne G., Kraus A., 2013, , 51, 269

Dunhill A. C., Cuadra J., Dougados C., 2015, , 448, 3545

Epstein P. S., 1924, Physical Review, 23, 710

Farris B. D., Duffell P., MacFadyen A. I., Haiman Z., 2014, , 783, 134

Forgan D. H., Ilee J. D., Meru F., 2018, , 860, L5

Fuente A., et al., 2017, , 846, L3

Fukagawa M., et al., 2004, , 605, L53

Fukagawa M., Tamura M., Itoh Y., Kudo T., Imaeda Y., Oasa Y., Hayashi S. S., Hayashi M., 2006, , 636, L153

Gaia Collaboration et al., 2016, A&A, 595, A1

Garufi A., et al., 2018, , 620, A94

Gonzalez J. F., Laibe G., Maddison S. T., 2017, , 467, 1984

Gratton R., et al., 2019, , 623, A140

Hashimoto J., et al., 2011, , 729, L17

Huang J., et al., 2018, , 869, L43

Isella A., et al., 2018, , 869, L49

Isella A., Benisty M., Teague R., Bae J., Keppler M., Facchini S., Pérez L., 2019, , 879, L25

Johansen A., Youdin A., 2007, , 662, 627

Johansen A., Andersen A. C., Brandenburg A., 2004, , 417, 361

Kennedy G. M., et al., 2019, Nature Astronomy, p. 189

Kwok S., 1975, , 198, 583

Lacour S., et al., 2016, A&A, 590, A90

Lada C. J., 1987, in Peimbert M., Jugaku J., eds, IAU Symposium Vol. 115, Star Forming Regions. p. 1

Laibe G., Price D. J., 2012a, , 420, 2345

Laibe G., Price D. J., 2012b, , 420, 2365

Langlois M., et al., 2018, , 614, A88

Lubow S. H., Martin R. G., 2018, , 473, 3733

Lyra W., Lin M.-K., 2013, , 775, 17

Marino S., Perez S., Casassus S., 2015, ApJL, 798, L44

Martin R. G., Lubow S. H., 2017, , 835, L28

Meheut H., Meliani Z., Varniere P., Benz W., 2012, , 545, A134

Miranda R., Lai D., 2015, , 452, 2396

Montesinos M., Cuello N., 2018, , 475, L35

Montesinos M., Perez S., Casassus S., Marino S., Cuadra J., Christiaens V., 2016, , 823, L8

Nakagawa Y., Sekiya M., Hayashi C., 1986, , 67, 375

Nixon C. J., Cossins P. J., King A. R., Pringle J. E., 2011, , 412, 1591

Nixon C., King A., Price D., 2013, , 434, 1946

Owen J. E., 2016, Publications of the Astronomical Society of Australia, 33, e005

Owen J. E., Kollmeier J. A., 2017, , 467, 3379

Pacheco-Vázquez S., et al., 2016, , 589, A60

Perez S., et al., 2015, , 798, 85

Pérez L. M., et al., 2016, Science, 353, 1519

Pérez S., Casassus S., Baruteau C., Dong R., Hales A., Cieza L., 2019, , 158, 15

Pinilla P., et al., 2018, , 859, 32

Pinte C., et al., 2018, , 860, L13

Pirzkal N., Spillar E. J., Dyck H. M., 1997, , 481, 392

Pohl A., et al., 2017, , 850, 52

Price D. J., 2007, Publications of the Astronomical Society of Australia, 24, 159

Price D. J., et al., 2018a, Publications of the Astronomical Society of Australia, 35, e031

Price D. J., et al., 2018b, , 477, 1270

Raghavan D., et al., 2010, The Astrophysical Journal Supplement Series, 190, 1

Ragusa E., Dipierro G., Lodato G., Laibe G., Price D. J., 2017, Monthly Notices of the Royal Astronomical Society, 464, 1449

Reipurth B., Clarke C. J., Boss A. P., Goodwin S. P., Rodríguez L. F., Stassun K. G., Tokovinin A., Zinnecker H., 2014, in Beuther H., Klessen R. S., Dullemond C. P., Henning T., eds, Protostars and Planets VI. p. 267 (arXiv:1403.1907), doi:10.2458/azu˙uapress˙9780816531240-ch012

Rivière-Marichalar P., Fuente A., Baruteau C., Neri R., Treviño-Morales S. P., Carmona A., Agúndez M., Bachiller R., 2019, The Astrophysical Journal, 879, L14

Rodríguez L. F., Zapata L. A., Dzib S. A., Ortiz-León G. N., Loinard L., Macías E., Anglada G., 2014, , 793, L21

Shi J.-M., Krolik J. H., Lubow S. H., Hawley J. F., 2012, , 749, 118

Stepinski T. F., Valageas P., 1996, , 309, 301

Stolker T., et al., 2016, , 595, A113

Takeuchi T., Lin D. N. C., 2002, , 581, 1344

Tang Y. W., Guilloteau S., Piétu V., Dutrey A., Ohashi N., Ho P. T. P., 2012, , 547, A84

Tang Y.-W., et al., 2017, , 840, 32

Testi L., et al., 2014, in Beuther H., Klessen R. S., Dullemond C. P., Henning T., eds, Protostars and Planets VI. p. 339 (`arXiv:1402.1354`), doi:10.2458/azu˙uapress˙9780816531240-ch015

Tokovinin A., 2014, , 147, 86

Tsukagoshi T., et al., 2016, , 829, L35

Weidenschilling S. J., 1977, , 180, 57

Williams J. P., Cieza L. A., 2011, , 49, 67

Zanazzi J. J., Lai D., 2018, , 473, 603

van der Marel N., et al., 2013, Science, 340, 1199

van der Marel N., van Dishoeck E. F., Bruderer S., Andrews S. M., Pontoppidan K. M., Herczeg G. J., van Kempen T., Miotello A., 2016a, , 585, A58

van der Marel N., Cazzoletti P., Pinilla P., Garufi A., 2016b, , 832, 178

van der Plas G., et al., 2019, , 624, A33